Pacheco *et al. Earth, Planets and Space (2024) 76:79*
https://doi.org/10.1186/s40623-024-02022-7

Earth, Planets and Space

FULL PAPER

Open Access

The impact of the Hunga Tonga–Hunga Ha'apai volcanic eruption on the Peruvian atmosphere: from the sea surface to the ionosphere

E. E. Pacheco[1*], J. P. Velasquez[1], R. Flores[1], L. Condori[1], G. Fajardo[1,2], K. Kuyeng[1], D. E. Scipion[1], M. Milla[3], J. F. Conte[4], F. L. Poblet[4], J. L. Chau[4], J. Suclupe[1,4], R. Rojas[1] and E. Manay[1]

Abstract

The eruption of the Hunga Tonga Hunga Ha'apai volcano on 15 January 2022 significantly impacted the lower and upper atmosphere globally. Using multi-instrument observations, we described disturbances from the sea surface to the ionosphere associated with atmospheric waves generated by the volcanic eruption. Perturbations were detected in atmospheric pressure, horizontal magnetic field, equatorial electrojet (EEJ), ionospheric plasma drifts, total electron content (TEC), mesospheric and lower thermospheric (MLT) neutral winds, and ionospheric virtual height measured at low magnetic latitudes in the western South American sector (mainly in Peru). The eastward Lamb wave propagation was observed at the Jicamarca Radio Observatory on the day of the eruption at 13:50 UT and on its way back from the antipodal point (westward) on the next day at 07:05 UT. Perturbations in the horizontal component of the magnetic field (indicative of EEJ variations) were detected between 12:00 and 22:00 UT. During the same period, GNSS-TEC measurements of traveling ionospheric disturbances (TIDs) coincided approximately with the arrival time of Lamb and tsunami waves. On the other hand, a large westward variation of MLT winds occurred near 18:00 UT over Peru. However, MLT perturbations due to possible westward waves from the antipode have not been identified. In addition, daytime vertical plasma drifts showed an unusual downward behavior between 12:00 and 16:00 UT, followed by an upward enhancement between 16:00 and 19:00 UT. Untypical daytime eastward zonal plasma drifts were observed when westward drifts were expected. Variations in the EEJ are highly correlated with perturbations in the vertical plasma drift exhibiting a counter-equatorial electrojet (CEEJ) between 12:00 and 16:00 UT. These observations of plasma drifts and EEJ are, so far, the only ground-based radar measurements of these parameters in the western South American region after the eruption. We attributed the ion drift and EEJ perturbations to large-scale thermospheric wind variations produced by the eruption, which altered the dynamo electric field in the Hall and Pedersen regions. These types of multiple and simultaneous observations can contribute to advancing our understanding of the ionospheric processes associated with natural hazard events and the interaction with lower atmospheric layers.

Keywords Volcanic eruption, Hunga Tonga–Hunga Ha'apai volcano, Tonga, Equatorial ionosphere, Tonga eruption effects, Peruvian ionosphere, Barometer, Magnetometer, Coherent radar, Perturbation waves, Equatorial electrojet, 150-km echoes, Plasma drifts, Ionosonde, GNSS-TEC

*Correspondence:
E. E. Pacheco
epacheco@igp.gob.pe
Full list of author information is available at the end of the article

Graphical Abstract

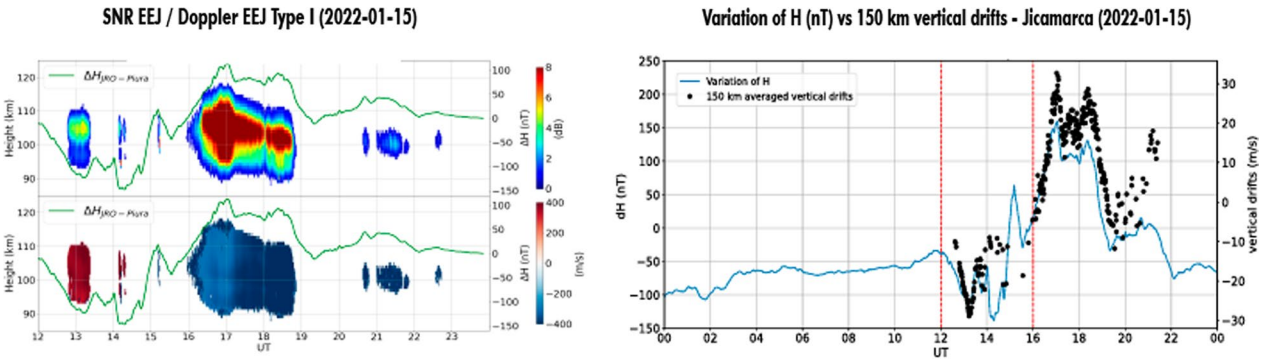

Introduction

Phenomena such as earthquakes, meteor air bursts, nuclear blasts, tsunamis, and volcanic eruptions can trigger traveling disturbances in the atmosphere that can be detected around the world (Calais and Minster 1998; Astafyeva 2019; Afraimovich et al. 2001, 2013; Artru et al. 2005; Azeem et al. 2017; Huang et al. 2019). The Hunga Tonga–Hunga Ha'apai underwater volcano (20.53° S 175.38° W UT+13) erupted 5 times during the period corresponding to 15 January 2022 from 04:05 UT and 04:54 UT (Astafyeva et al. 2022). The main explosion occurred at 04:18 UT, releasing an amount of energy equivalent to a range between 9 and 37 Megaton of TNT and produced the propagation of mechanical waves from below the ocean surface to the ionosphere (Adam 2022; Wright et al. 2022), where part of the energy traveled across the ocean and part through the atmosphere. The enormous amount of energy released produced tsunami waves, gravity waves, acoustic waves, infrasound waves, and Rossby waves that generated geophysical variations across the Earth's atmosphere (Amores et al. 2022). From all these, those expected to propagate long distances were the acoustic waves and Lamb waves (Nishida et al. 2014). Atmospheric pressure disturbances traveled in the form of Lamb waves and surrounded the Earth several times. The volcano eruption can produce effects in the lower atmosphere (varying atmospheric pressure), in the mesosphere and lower thermosphere (MLT) region (modifying neutral winds), as well as in the ionosphere (perturbing the horizontal magnetic field component—H, the vertical plasma drifts, the equatorial electrojet—EEJ, and the virtual height of the ionograms) (Poblet et al. 2023; Stober et al. 2023; Schnepf et al. 2022; Le et al. 2022; Sun et al. 2022; Li et al. 2023; Harding et al. 2022; Qiu et al. 2023).

Several studies have focused their efforts on characterizing atmospheric wave features associated with the Tonga event. Observations from GNSS data have been used to analyze the phase speed, period and frequency of traveling ionospheric disturbances (TIDs) that occurred after the eruption and were associated with the propagation of the Lamb wave (Themens et al. 2022; Zhang et al. 2022; Takahashi et al. 2023; Heki 2022). Zhang et al. (2022) observed ionospheric disturbances traveling three times around the globe using worldwide GNSS ground receivers measurements. Traveling ionospheric disturbances (TIDs) were detected propagating at speeds of about 300–350 m/s and with horizontal wavelengths of 500–1000 km for front shocks. Themens et al. (2022) used globally distributed GNSS receivers to track the propagation of traveling ionospheric disturbances (TIDs) after the eruption on 15 January 2022. They identified two main highly directional Large Scale traveling ionospheric disturbances (LSTIDs) with speeds of about 555–950 m/s within 3000 km of the epicenter and Medium Scale traveling disturbances (MSTIDs) with speeds of about 200–400 m/s. Takahashi et al. (2023) reported atmospheric pressure waves over South America between 12:30 and 17:30 UT, tsunamis along the Chilean coast between 17:00 and 19:00 UT, and ionospheric disturbances (TEC variations) between 11:30 and 20:00 UT propagating from Chile to the eastern South American sector. Heki (2022) observed ionospheric disturbances over Japan propagating as fast as the atmospheric Lamb wave, suggesting upward energy leakage from the troposphere as the source of these disturbances in ionospheric TEC (Francis 1973; Nishida et al. 2014).

Reports of perturbations in the MLT region have also shown signatures attributed to the volcano explosion. Utilizing three multistatic specular meteor radars spaced more than 3000 km apart, MLT horizontal wind disturbances were found over the west side of South America (Poblet et al. 2023). A notorious wave was identified

around 18 UT, with an amplitude of ~ 50 m/s mainly in the westward direction, traveling at ~ 200 m/s, with a period of ~ 2 h and a horizontal wavelength of ~ 1440 km in the longitudinal direction, away from the source. Observations from multistatic meteor radar networks in the western South American and northern European sectors were used to identify gravity waves in MLT winds caused by the volcano (Stober et al. 2023). Eastward- and westward-traveling gravity waves in zonal and meridional winds were found arriving 12 and 48 h after the eruption in the western South American region with an estimated intrinsic phase speed of about 200–212 m/s.

Other investigations have used satellite data from the Ionospheric Connection Explorer (ICON) (Immel et al. 2018) and SWARM (Friis-Christensen et al. 2006; Wood et al. 2022) supported by ground-based magnetometers in order to further study the effects of the perturbations in lower ionospheric layers (Harding et al. 2022). Their analysis of the EEJ and neutral winds measurements showed that a westward electrojet was driven by strong westward winds in the Pedersen region caused by the eruption. Le et al. (2022) observed a strong counter-electrojet (CEJ) after an enhanced EEJ associated with the volcano event using SWARM satellites and ground-based magnetometers in the South American sector. They proposed that this CEJ was associated with strong eastward turning of zonal winds in the E-region ionosphere and the intensification of EEJ was related to enhanced E-region westward zonal winds.

Furthermore, conjugate effects associated with the volcanic eruption have been reported recently. Lin et al. (2022) used GNSS-TEC measurement to notice the appearance of concentric TIDs in the Southern Hemisphere (Australia) and Northern Hemisphere (Japan) almost simultaneously through interhemispheric coupling, 3 h prior to the arrival of surface air pressure waves (Lamb wave) to Japan. Shinbori et al. (2022) observed the electromagnetic conjugacy of ionospheric disturbances in both Northern and Southern Hemispheres using GNSS-TEC and SuperDARN Hokkaido pair of radars measurements shortly after the volcano eruption. They found that TIDs, measured as TEC perturbations over Japan and Australia, appeared over Japan before the arrival of air pressure disturbances associated with the volcanic event. The amplitude and period of plasma flow variations coincident with the TIDs were about 100–110 m/s and 36–38 min, respectively. Gasque et al. (2022) showed evidence of ionospheric electrodynamic effects produced by the Hunga Tonga–Hunga Ha'apai volcano eruption in the Pacific sector. They reported extreme zonal and vertical $\mathbf{E} \times \mathbf{B}$ ion drift measured by ICON's Ion Velocity Meter within an hour of the main eruption (04:51–04:56 UT). Perturbations in the drift velocities were detected when the satellite was passing through the region 4000 km away from the eruption and that is magnetically connected to the E-region located at about 400 km from the volcano. These investigations have shown evidence of E-region dynamo electric field disturbances driven by neutral wind perturbations caused by the volcano eruption and the mapping of electric fields from the Southern to the Northern Hemisphere in the Pacific sector. However, no electric fields or plasma drifts perturbations due to the eruption have been observed over the western South American region in previous studies and compared with disturbances detected in other ionospheric parameters.

In this work, the effects produced by the Hunga Tonga–Hunga Ha'apai (hereafter Tonga) volcanic eruption in the Peruvian sector (atmospheric pressure, magnetic field, equatorial electrojet, plasma drifts, neutral MLT winds, and total electron content) are described and presented in a temporal sequence. This is the first time that the Jicamarca Radio Observatory radar has detected the impact of a volcanic eruption on the equatorial ionospheric electrodynamics over Peru. The paper describes the diverse effects produced in the Peruvian atmosphere observed by several types of instruments on the same day and the day after the volcanic eruption. The structure of the paper is organized as follows: in "Measurements" section, the measurements and observations carried out by all the instruments involved in this study are described. In "Analysis of temporal variations" section, the observations are arranged in a time sequence to show the effects detected in the instrumentation, their duration and its relation with other measurements, if any. Then, the perturbations observed in the measurements attributed to the eruption effect are interpreted and discussed. Finally, the summary and conclusions are presented.

Measurements

The response of the ionosphere to the Tonga volcanic eruption over the Peruvian sector caused perturbations in the signals and measurements conducted with different instruments. The instrumentation included magnetometers, a VHF radar system for oblique EEJ observations, the Jicamarca Radio Observatory (JRO) main radar (11.95° S, 76.87° W, 540.55 m), a multistatic specular meteor radar system, an ionosonde system, GPS receivers, and atmospheric pressure sensors. The analysis was mainly focused on the observations of 15 January 2022; however, additional days of measurements were considered to compare the unusual behavior of the atmospheric parameters due to the eruption with their typical behavior. The geographical location of the Jicamarca Radio Observatory and the Peruvian sector with respect to the epicenter of the eruption is given in Fig. 1a, the distance

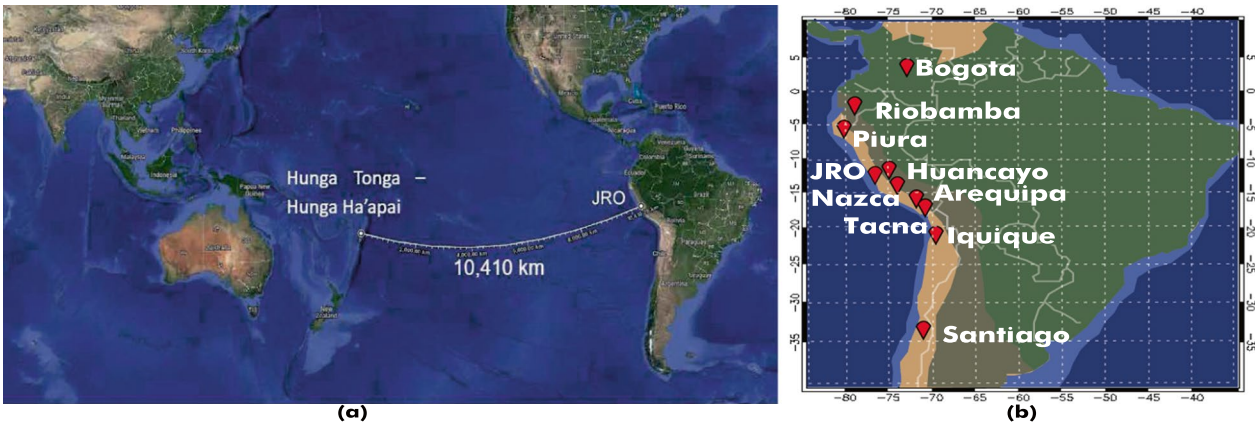

Fig. 1 **a** Location of the Jicamarca Radio Observatory, Lima, Peru, with respect to the Hunga Tonga–Hunga Ha'apai volcano. The distance from the eruption to Jicamarca is about 10,410 km. **b** Location of the ground-based stations (magnetometers, GPS receivers, radars, ionosonde, and barometers) used to analyze the volcanic effects in the western South American sector

between these locations is about 10,410 km. The multi-instrumental and simultaneous measurements carried out near the 76° W longitude at different altitudes enable us to describe the phenomena in a deeper and more comprehensive way. The location of the instruments used in this study is presented in Fig. 1b.

Atmospheric pressure

We used atmospheric pressure measurements from meteorological stations (barometers) located at the Jicamarca Radio Observatory (11.95° S, 76.87° W), the University of Piura (5° S, 80° W), and the Huancayo Observatory (12.04° S, 75.32° W). Their corresponding time resolution is 5, 10, and 2 min, respectively. In order to isolate the effects of the propagation of the mechanical waves produced by the eruption, the atmospheric pressure anomaly (APA) has been calculated by averaging the measurements of the unperturbed days and subtracting it from daily measurements for 15–16 January.

The arrival of two wave fronts of great magnitude was observed on 15 January as shown in the green curve of Fig. 2 (peak at 13:50 UT, starting at 13:40 UT), and on 16 January (07:05 UT, starting at 06:55 UT), approximately 25 h 45 m after the eruption (red curve). The first wave front would correspond to the propagation of disturbances from Tonga to its antipodal point (North Africa) in the west–east direction, while the second one would correspond to the waves traveling in the opposite direction, from east to west. Two additional days (14 and 17) of Jicamarca data are displayed in Fig. 2, in order to compare the perturbed measurements with those corresponding to the day before and two days after the eruption when no perturbations were seen.

On 15 January, the Piura, Jicamarca, and Huancayo stations detected the peak of the pressure anomaly at 13:40, 13:50, and 14:00 UT, respectively, as shown in Fig. 3. The sequence of detection is consistent with the distances from Tonga to each station, with Piura as the closest one in the west–east direction. The wave that passed through the antipode (east to west) reached the Peruvian sector on 16 January near 07:00 UT as shown in Fig. 4.

It is important to note that tsunami waves were detected after the arrival of the atmospheric pressure anomalies in the South American Pacific coast (Carvajal et al. 2022; Takahashi et al. 2023; Ravanelli et al. 2023). The arrival of tsunamis leading waves on the Peruvian coast was observed near 14:30 UT and 15:30 UT for Matarani (17.0009° S, 72.1088° W) and Callao (12.096° S, 77.1668° W), respectively (Figure S1 in Supplementary information). After the leading waves, larger amplitudes of tsunami occurred with the corresponding initial times near 19:00 UT. The ocean sea level data sets are available from the sea level observing system UNESCO/Intergovernmental Oceanic Commission (IOC).

Magnetometers

Digital magnetometers from the Low-Latitude Ionospheric Sensor Network (LISN) (Valladares and Chau 2012), based on fluxgate sensors of three components (XYZ), measured the variations of the geomagnetic field vector during the days around the volcanic eruption (http://lisn.igp.gob.pe/jdata/database/). A comparison of the horizontal component of the magnetic field (H) at different consecutive days around 15 January was carried out. We used the value of H at 05:00 UT on 13 January as our reference, considering the time before the beginning of the storm, and subtracted the H component for

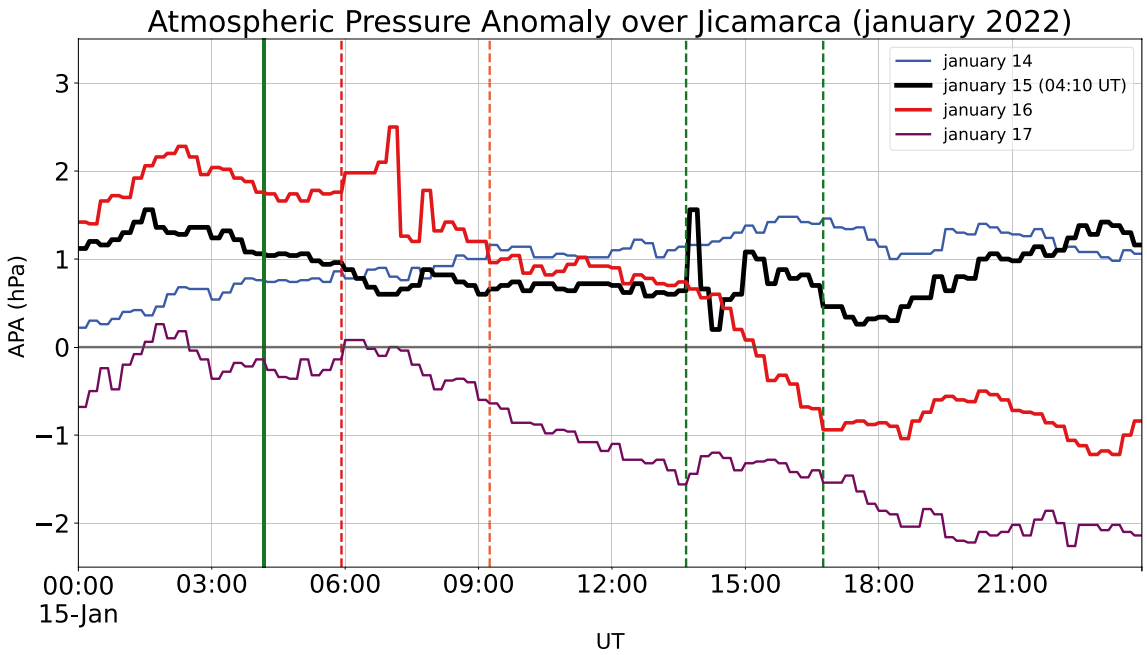

Fig. 2 Atmospheric pressure anomaly at the Jicamarca Radio Observatory on 14, 15, 16, 17 January 2022. The vertical solid green line corresponds to the time of the eruption (15 Jan 04:10 UT), whereas the green dashed lines indicate the time interval when the first wave front was detected on 15 January (13:40 to 16:45 UT) and the red dashed lines correspond to the arrival of the second wave front on 16 January (05:55 to 09:15 UT)

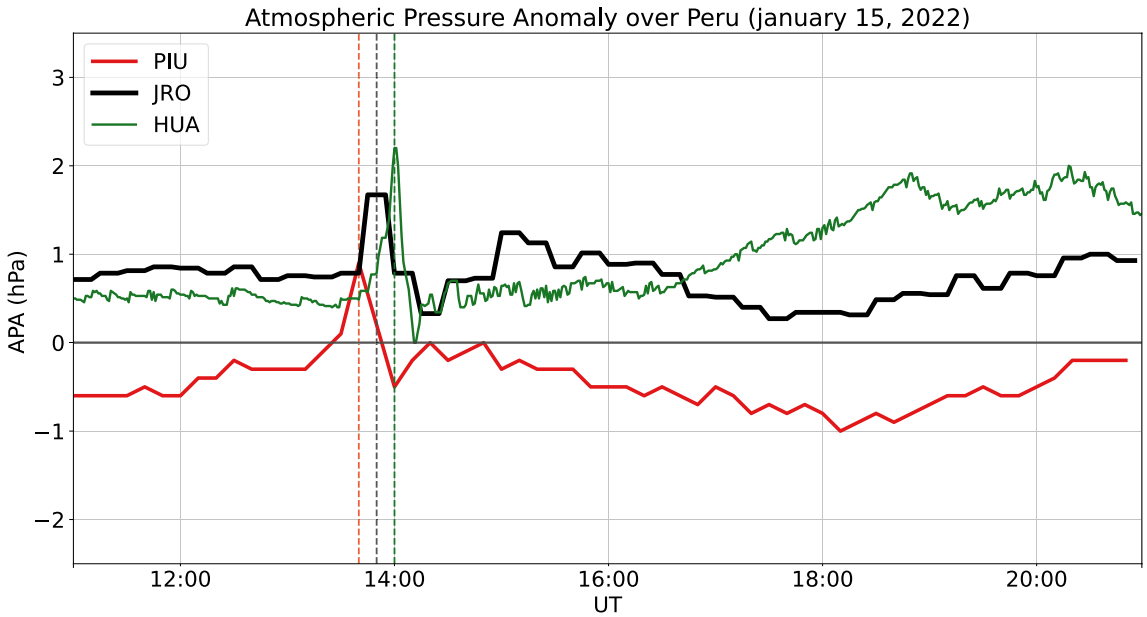

Fig. 3 Atmospheric pressure anomaly on 15 January over Piura, Jicamarca and Huancayo. The red dashed line corresponds to the arrival time of the first wave train at Piura, at 13:40 UT, whereas the black and green dashed lines represent the arrival time at Jicamarca, at 13:50 UT, and Huancayo, at 14:00 UT, respectively

each day (dH). A monthly-average variation of H for the month of January 2022 was estimated by taking 1-h intervals of data in the month's five quietest days to perform the average and standard deviation calculation. The value of H at 05:00 UT on 13 January was taken as a reference value and subtracted the H component for each day (dH).

An unusual behavior of H during the days 14 and 15 is observed in comparison to unperturbed days such as

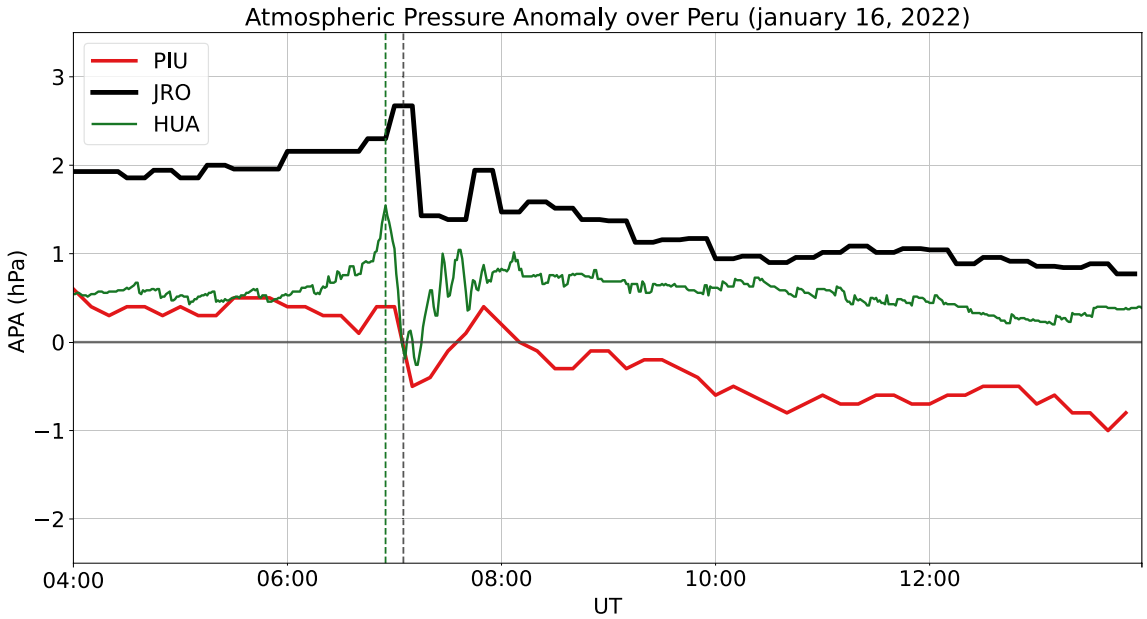

Fig. 4 Atmospheric pressure anomaly at Piura, Jicamarca, and Huancayo on 16 January 2022. The green dashed line represents the arrival time of the second wave train at Huancayo (green curve) and Piura (red curve), both has its peak at 06:55 UT, whereas the black dashed line indicates the arrival time at Jicamarca (black curve), with a peak at 07:05 UT

13, 16, and 17, and the monthly-average of January as shown in Fig. 5. A G1 and G2 class geomagnetic storm started on 14 January, disturbing the measured values of H at the end of the day. By the time of the Tonga eruption, on 15 January, the storm entered its recovery phase, which is the last stage of a geomagnetic storm when the Dst index increases from its minimum value to its quiet time value and it might last from 8 h to 7 days (Gonzalez et al. 1994). At about the time of the arrival of the acoustic wave in Peru, a strong decrease in the H component is distinguished (between 12:00 and 16:00 UT). That is likely due to ionospheric current intensity and direction changes, predominantly EEJ variations, which generally contribute to the magnetic field variability during the day. The origin of the disturbances observed in the EEJ was discarded as caused by the geomagnetic storm by

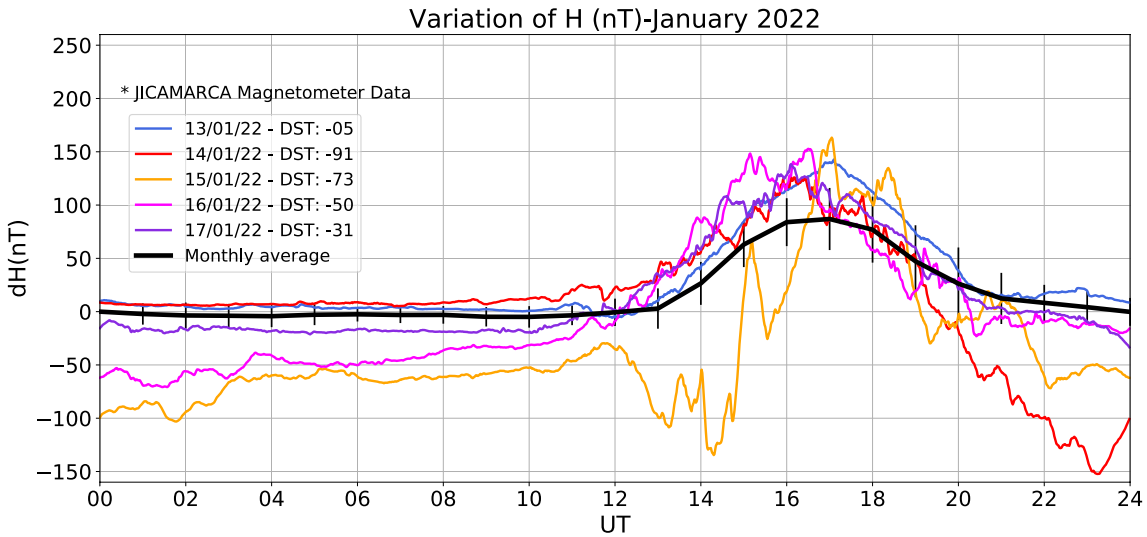

Fig. 5 Diurnal variation of the H magnetic field component (dH) measured at Jicamarca between 13–17 January 2022. A strong decrease in the H component is clearly distinguished on 15 January (between 12:00 and 16:00 UT)

Harding et al. (2022); hence, the perturbations seen in H are unrelated to the storm. The initial time of this disturbance was detected 1.6 h before the perturbations were measured by the barometer (atmospheric pressure).

Diurnal variations of H were measured by several magnetometer stations at Piura, Jicamarca, Huancayo, Nazca, and Arequipa on 15 January 2022 as illustrated in Fig. 6. A similar disturbance pattern appears simultaneously in all the magnetic stations but with different amplitudes. The largest amplitudes were observed at the stations near the magnetic equator (Jicamarca and Huancayo).

Equatorial electrojet

The difference of H between Jicamarca and Piura stations ($\Delta H_{\text{JRO-Piura}}$) gives us the contribution of the EEJ current (eastward propagation) to H in our equatorial station at Jicamarca (positive values) (Anderson et al. 2004). In addition, a 50-MHz VHF radar located at Jicamarca is used to observe the EEJ region. The antenna array of this radar is composed of 16 Yagi antennas and points obliquely to 53° toward the west direction. The radar is used to estimate EEJ parameters such as the Doppler shift and the spectral width for Type I and II echoes (Farley 1985). Every minute, the spectrum is fitted to a double Gaussian model at each range. Then, range–time intensity (RTI) plots are constructed to visualize the SNR, the direction and the intensity of the Doppler shift of Type I echoes.

The intensity of the EEJ current is represented by $\Delta H_{\text{JRO-Piura}}$, as shown in Fig. 7 (green curve). On the other hand, counter-electrojet (CEEJ) currents, westward propagation, generate negative values of $\Delta H_{\text{JRO-Piura}}$, which is what happened after the Tonga eruption. The signal-to-noise ratio of the EEJ obtained from radar echoes is also illustrated. At 12:46 UT a CEEJ echo was detected, this type of echo persisted until 13:24 UT and it is related to the change of sign of $\Delta H_{\text{JRO-Piura}}$. Later on, two 5-min-duration CEEJ echoes were detected near 14:08 UT and 14:14 UT, respectively. These observations agree with the abrupt decay of $\Delta H_{\text{JRO-Piura}}$ after it started to recover following the first CEEJ appearance.

The Doppler shift values of the EEJ type I echoes are presented in Fig. 7 (bottom panel), where red color means westward propagation of the EEJ current, while blue color indicates eastward propagation. It can be seen that westward propagation relates to negative $\Delta H_{\text{JRO-Piura}}$ values, and eastward propagation relates to positive $\Delta H_{\text{JRO-Piura}}$ values. Moreover, negative Doppler shifts change considerably throughout the day, but they vary slightly in range in each timestamp.

150-km echoes drifts

Coherent backscatter radar measurements of the Doppler velocity of the so-called 150-km echoes can provide a proxy of ionospheric vertical and zonal plasma drift estimates during daytime hours (Kudeki and Fawcett 1993; Chau and Woodman 2004). The height-averaged vertical and zonal drifts were obtained from 150-km radar echoes over Jicamarca. The measurements corresponding to the eruption day have been compared to a data set consisting of measurements from November 2021, December 2021, January 2022 (except for the eruption day) and February 2022. The height-averaged vertical and zonal drifts corresponding to the eruption day displayed a significant

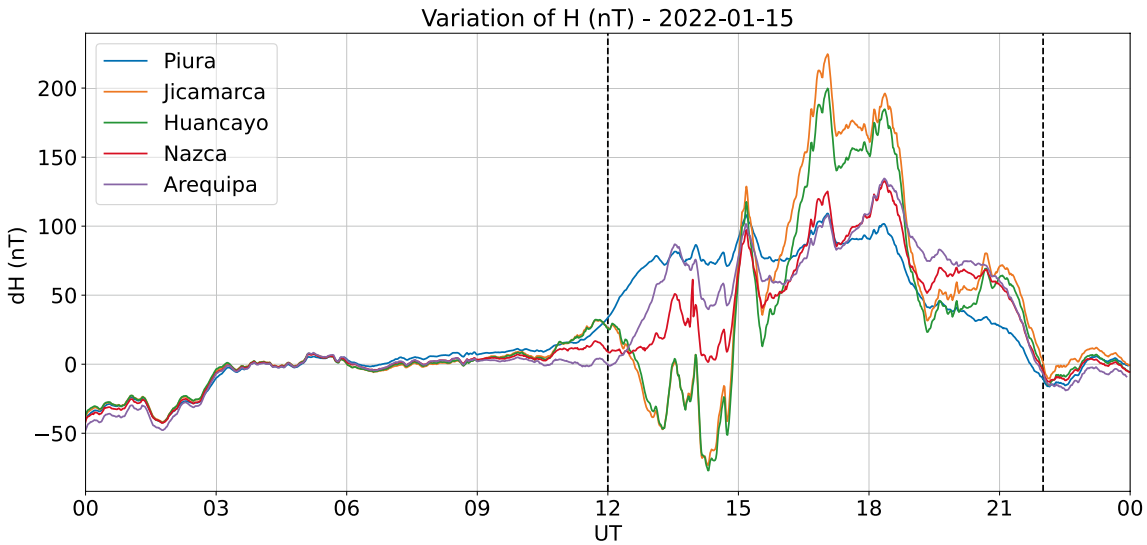

Fig. 6 Diurnal variation of the H magnetic field component (dH) measured by magnetometer stations at Piura, Jicamarca, Huancayo, Nazca, and Arequipa on 15 January 2022. The black dashed vertical lines indicate the beginning and ending time of the observed effects

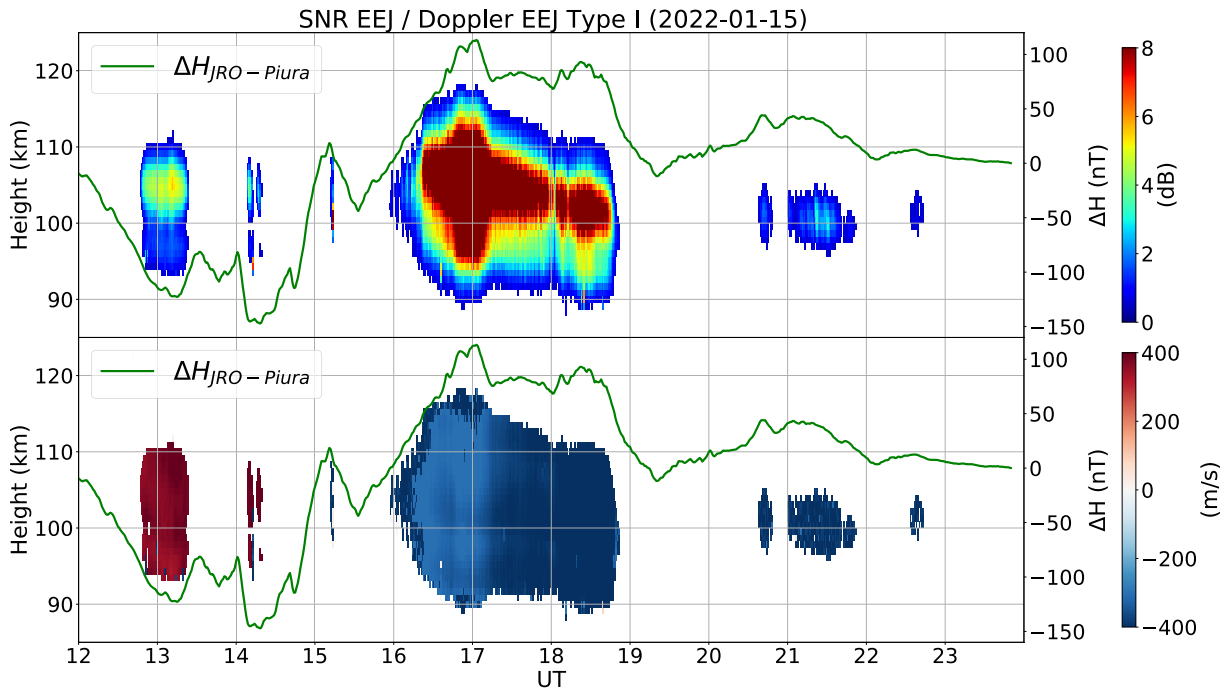

Fig. 7 Signal-to-noise ratio of EEJ echoes (upper panel) and Doppler shift (bottom panel) of EEJ type I echoes compared to the difference of the horizontal component of the magnetic field H between Jicamarca and Piura stations ($\Delta H_{\text{JRO-Piura}}$) on 15 January 2022

deviation from the average and the 5–95 percentile from a data set that includes measurements from November 2021, December 2021, January 2022, and February 2022 as shown in Fig. 8. Untypical daytime downward drifts of about −20 m/s were observed between 12:00 and 16:00 UT, followed by an enhanced upward drift of about 20 m/s between 16:00 and 18:00 UT. The magnitudes of these upward drifts were larger than the average values for that local time range. Between 19:00 and 21:00 UT, a minor reversal of the vertical drift (upward to downward)

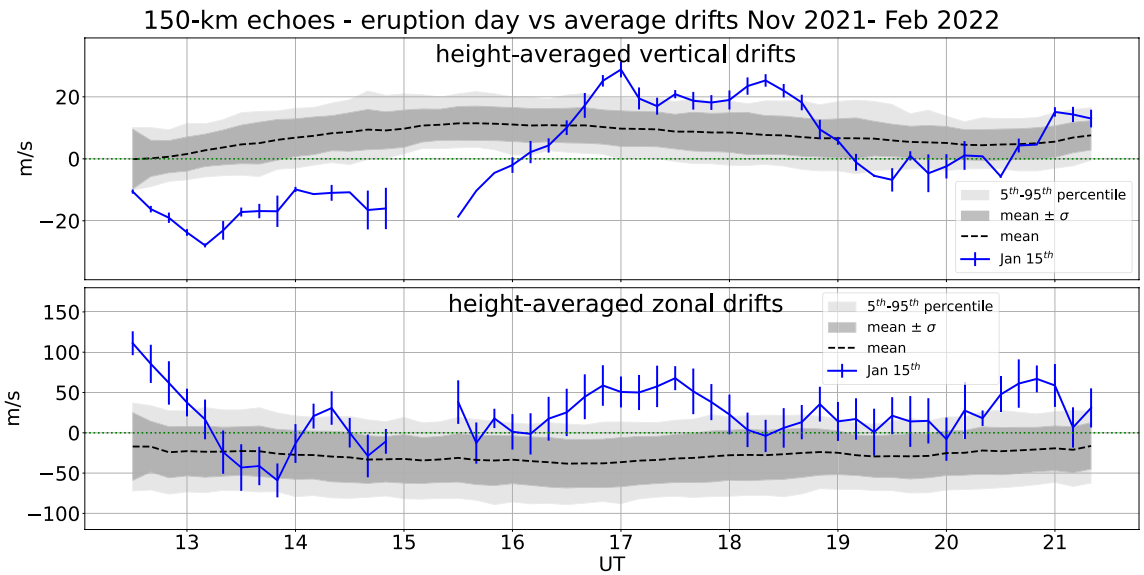

Fig. 8 150-km echoes height-averaged vertical (top) and zonal (bottom) drifts obtained on 15 January 2022 compared to 5% percentile, 95% percentile, and the mean. The vertical bars represent the standard deviation of the measurements for each 10-min interval

was observed. Unusual daytime eastward zonal plasma drifts were distinguished during the daytime, when typically westward drifts are expected.

The signatures observed in H and 150-km echoes vertical drifts are time-like consistent with each other as shown in Fig. 9.

Total electron content (TEC)

TEC measurements from GPS receiver stations nearby the western South American sector have been collected from the LISN and IGS networks. Table 1 summarizes the information corresponding to the stations involved in this work.

In order to isolate the perturbations δ_{TEC} due to the volcanic eruption, a 5th-order low-pass Butterworth filter was applied to the TEC values for each station and this result was subtracted from the absolute TEC to obtain the perturbations as a function of time. A Savitzky–Golay filter was applied to this result to obtain the final δ_{TEC} (Savitzky and Golay 1964; Zhang et al. 2022).

On 15 January, fluctuations in TEC variation were observed by GPS receivers at different latitudes in the west South American region near the Peruvian sector after 12:00 UT as shown in Fig. 10. The panels are organized from top to bottom from the closest to the farthest station with respect to Tonga. The distance in kilometers is indicated next to the location of each station. The vertical blue line near 04:18 UT represents the volcano eruption time. The second blue line near 13:40 UT represents the beginning of the fluctuations in TEC associated with the eruption. On the first panel, corresponding to the Santiago station, a first wave of TEC disturbances started near 12:00–14:00 UT. The stations closer to the eruption detected the perturbations first. The propagation time of the wave since the occurrence of the eruption is about 9 h approximately. A second wave train that is more evident at the Santiago, Iquique, Arequipa, and Tacna stations started around 18:00 UT. These perturbations persisted until 24:00 UT, however a similar behavior was observed between 22:00 and 24:00 UT on the

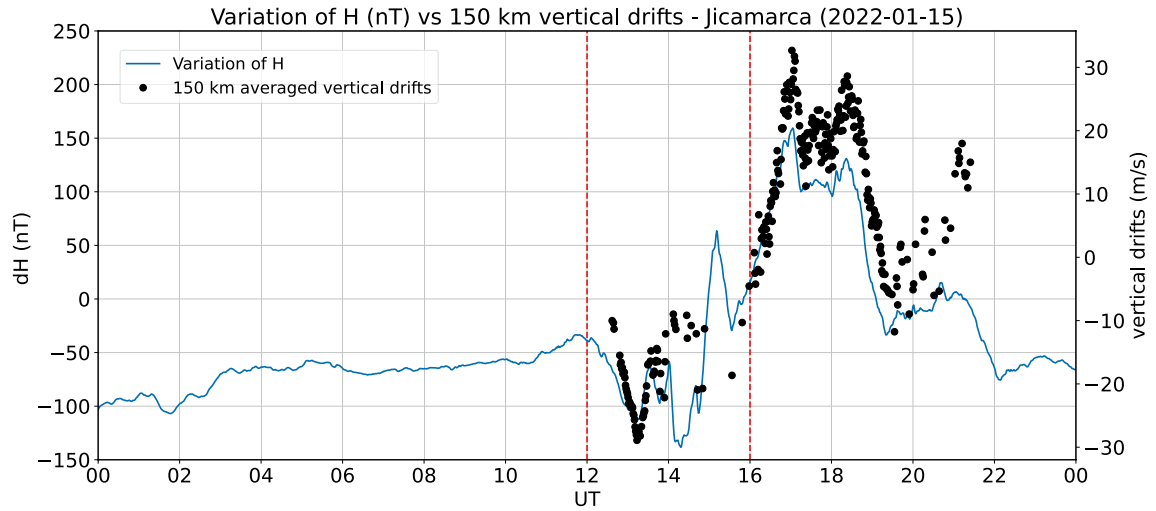

Fig. 9 Variation of H compared with the height-averaged 150-km echoes vertical drifts obtained on 15 January 2022 over Jicamarca. The red dashed vertical lines indicate the interval when CEEJ was observed

Table 1 GPS receivers used to measure TEC variations

GPS station	GPS model	Location (lat, lon, alt)	Network
Santiago (SANT00CHL)	SEPT POLARX5	−33.150, −70.669, 723 m	IGS
Jicamarca (jro)	SEPT POLARX5	−11.95, −76.87, 539 m	LISN
Huancayo (hyo)	Novatel GPS-702	−12.04, −75.32, 3321 m	LISN
Iquique (IQQE00CHL)	TRIMBLE NETR9	−20.274, −70.132, 39 m	IGS
Riobamba (RIOP00ECU)	TRIMBLE NETRS	−1.651, −78.651, 2793 m	IGS
Arequipa (AREQ00PER)	SEPT POLARX5	−16.466, −71.493, 2489 m	IGS
Tacna (tac)	Novatel GPS-702	−18.0, −70.22, 639.26	LISN
Bogotá (BOGT00COL)	JAVAD TRE_3 DELTA	4.640, −74.081, 2577 m	IGS

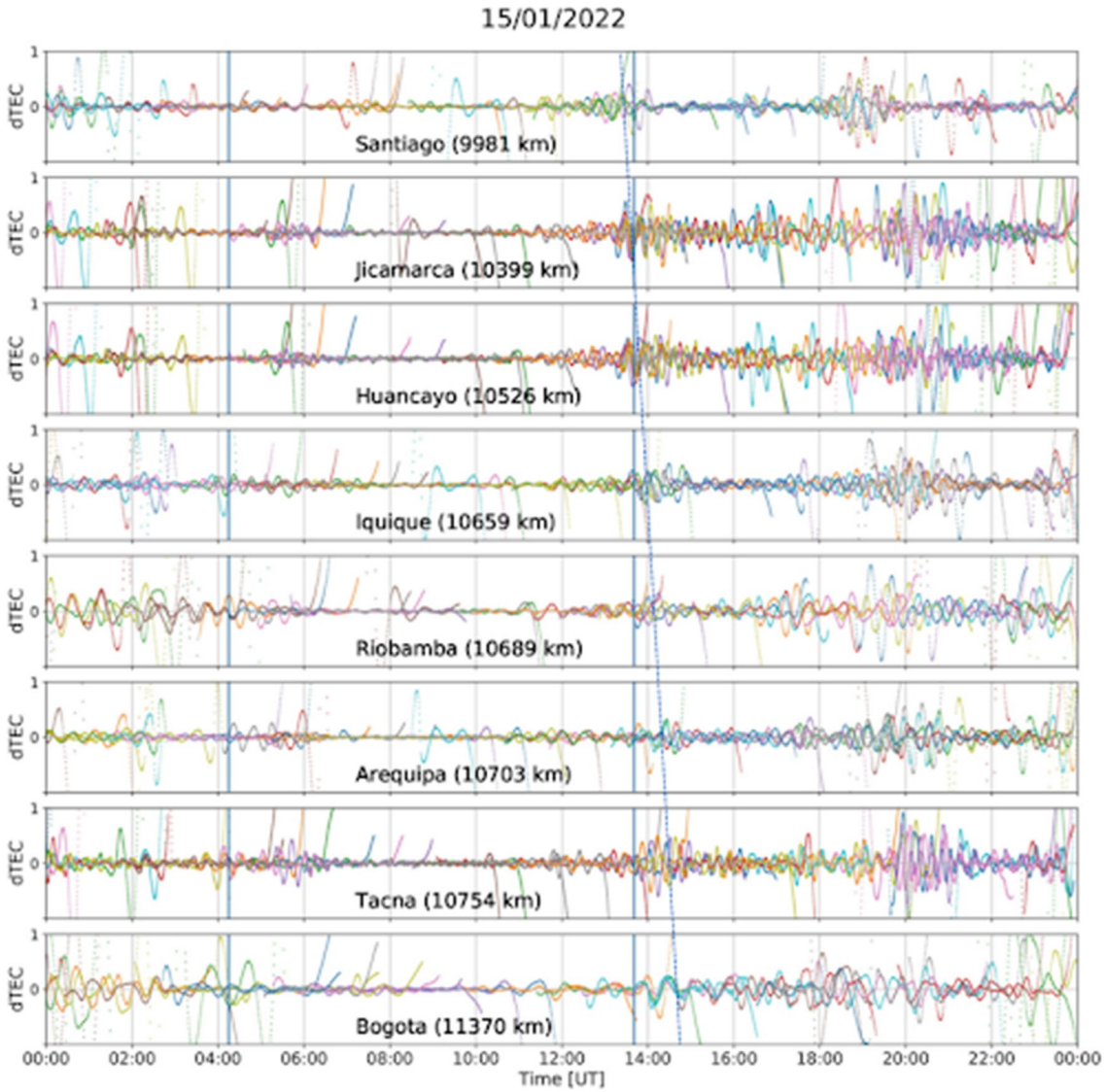

Fig. 10 TEC variation at different latitudes in the western South American sector on 15 January 2022. The value indicated next to the station name represents the distance from the epicenter of the eruption to each station. The first blue vertical line represents the hour of the Tonga volcano eruption. The second blue line represents the approximate arrival time of the perturbation to the Jicamarca station considering the wave propagates near the speed of sound. The dashed line shows the approximate arrival time of the perturbation at each station. The different colors in dTEC indicate the signals corresponding to different GPS satellites

previous and following days (13, 14, 16 and 17 January) hence they might not be related to the volcanic eruption. Quasi-periodic oscillations with periodicities ranging from about 15 to 40 min were found in the TEC fluctuations, representing signatures of possible traveling ionospheric disturbances.

Ionosonde

The vertical incidence pulsed ionospheric radar (VIPIR) ionosonde, located at JRO, is a fully digital frequency agile radar that probes the ionosphere vertically with signals of frequencies ranging from 0.3 to 25 MHz (Valladares and Chau 2012). It provides highly precise measurements of the ionospheric critical frequency (foF2), the height of F2 maximum electron density (hmF2), virtual heights (h'F), and electron density profiles.

According to Pradipta et al. (2015), a strong mechanical disturbance in the atmosphere such as a nuclear explosion, a tsunami, a meteor air burst, an earthquake, or a volcanic eruption can produce a Y-forking signature in the ionograms. Ionograms were visually inspected to detect unusual behavior of the ionosphere related to the

Tonga eruption such as this Y-forking signature. On 15 January 2022, these signatures were observed between approximately 20:13 UT and 22:00 UT with the VIPIR ionosonde over Jicamarca. An example of an unusual Y-forking pattern is shown in Fig. 11. This type of signature is untypical over Jicamarca, therefore this feature should be associated with the appearance of TIDs propagating in the ionosphere. Some other ionospheric parameters showed perturbations during this period. Near 20:00 UT, we observe the largest TEC fluctuations at the GNSS stations, as shown in the previous section. On the other hand, at about this time, plasma drifts and EEJ current intensity decreased to small magnitudes.

Neutral winds in the mesosphere and lower thermosphere (MLT)

Measurements of zonal and meridional neutral winds in the MLT region, between 80 and 100 km altitude, were obtained using the Spread-spectrum Interferometric Meteor Observing Network (SIMONe). One multistatic specular meteor radar system at the central part of Peru is SIMONe-Jicamarca (Chau et al. 2021). This system has one 5-antenna transmitter station located at the JRO (11.95° S, 76.87° W, 540.55 m) and five spaced receiver stations located at a range between 30 and 180 km from JRO. Another SIMONe system with a 6-antenna transmitter and six single antenna receiving stations, named SIMONe-Piura, is operating in northern Peru, where its transmitter is located at the Universidad de Piura (UdeP) (5.17° S, 80.64° W, 50.59 m). We obtained 1-h, 2-km zonal (u) and meridional (v) neutral winds over Jicamarca on the eruption day as a function of altitude and time. The variation of zonal and meridional winds with respect to 4-h mean values was calculated to identify the perturbations on MLT winds associated with the Tonga event.

The first row of Fig. 12 shows the 1-h, 2-km zonal (u) and meridional (v) neutral winds over Jicamarca. The 4-h mean values of the winds are presented in the second row. And the third row shows the difference between the first and the second rows that allow us to detect the wind perturbations. The largest variation that might be related to the effect of the Tonga volcanic eruption occurred at 18:00 UT. That instant is indicated with the cyan dashed vertical line. About that time, a zonal wind change from eastward to westward above 95 km altitude was observed; however, this large negative variation can be distinguished from 80 to 100 km approximately. Similar features were observed in MLT wind measurements over Piura as shown in Fig. 12, but in this case the change of the zonal wind from eastward to westward is noticed between 90 and 100 km altitude. The wind perturbation shows that the negative variation (change from eastward to westward) is much more clearly appreciated at a more extended range of altitudes. In fact, the change extends over approximately the same altitude range at both locations from 80 to 100 km. Besides, in that row, the effect from expected large-scale waves, such as tides and planetary waves, is removed by the 4-h mean. Thus, we have better chances that the observed east-to-west sudden change is indeed related to the Tonga event. On the other hand, MLT perturbations over Peru due to possible westward waves from the antipode on January 16 have not been identified.

A summary of the measurements and instruments used is shown in Table 2.

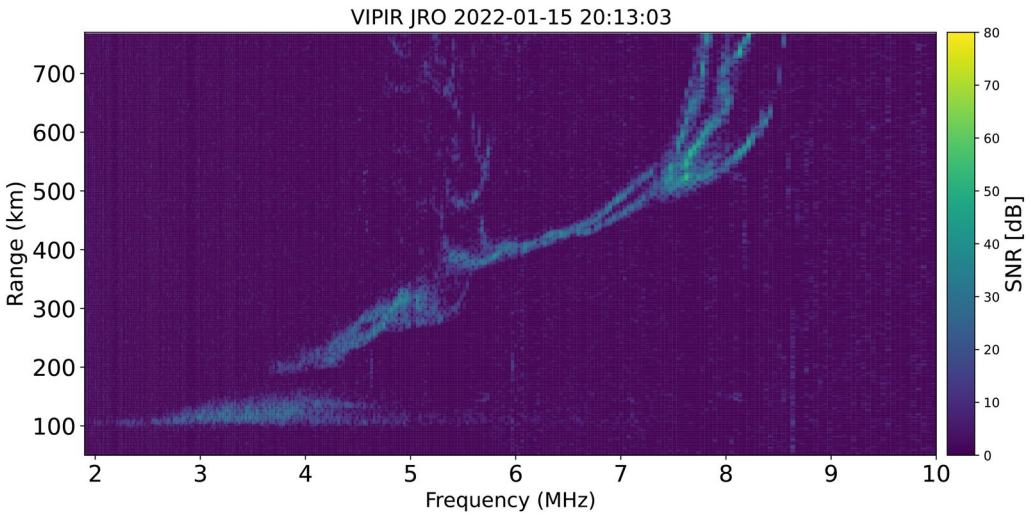

Fig. 11 Example of an unusual Y-forking signature corresponding to a TID passing above the Jicamarca Radio Observatory

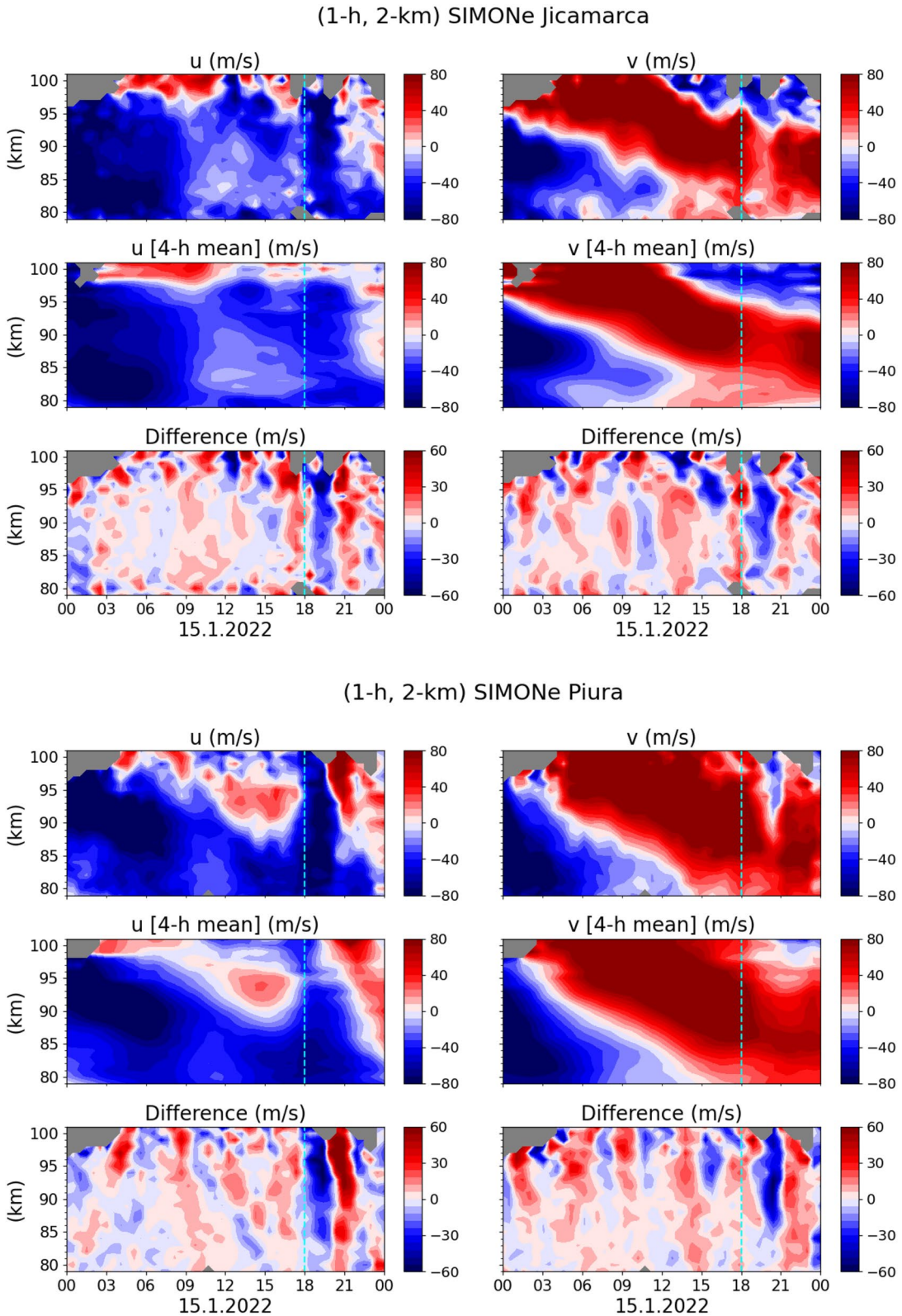

Fig. 12 Zonal and meridional winds between 80 and 100 km altitude from the SIMONe system over Jicamarca and Piura as a function of UT on 15 January. The cyan line at 18:00 UT indicates the beginning of the variations on the wind estimates possibly associated with the Tonga volcanic eruption

Table 2 Summary of the data utilized in this work

	Atmospheric pressure	**Magnetometer *H* variation**	**TEC**		**EEJ**	**150-km echoes vertical drifts**	**MLT Winds**	**Ionograms**
Stations	Jicamarca Radio Observatory (JRO) barometer (GLON 283°, GLAT −11.95°)	Piura (GLAT −5.19°) Jicamarca (GLAT −11.95°) Huancayo (GLAT −12.06°) Nazca (GLAT −14.83°) Arequipa (GLAT −16.39°)	Bogota (GLAT 4.609°) Riobamba (GLAT −1.67°) Jicamarca (GLAT −11.95°) Huancayo (GLAT −12.06°)	Arequipa (GLAT −16.39°) Tacna (GLAT −18.20°) Iquique (GLAT −20.21°) Santiago (GLAT −33.45°)	JRO radar	JRO radar	SIMONe Jicamarca SIMONe Piura	JRO VIPIR ionograms
Period	14, 15, 16, 17 Jan	13, 14, 15, 16, 17 Jan	15 Jan	15 Jan	15 Jan	15 Jan	15 Jan	15 Jan
Description	The atmospheric pressure average of the previous days of the eruption is subtracted from the absolute value for each day	Variation of H compared to the value of H at 13 Jan, 5 UT	A Butterworth filter of 5th order is applied to the TEC values for each station and this result is subtracted from the absolute TEC to obtain the perturbations as a function of time. A Savitzky–Golay filter was applied to this result		The EEJ spectrum is fitted by using a double Gaussian function	Doppler shift of the 150-km echoes	Variation of zonal and meridional winds with respect to 4-h mean values	Detection of unusual characteristics of ionograms and Y-forking signature

Analysis of temporal variations

We found perturbations associated with the Tonga volcanic eruption occurring on 15 January 2022 in several physical parameters at different atmospheric layers and times, from the sea surface level passing through the mesosphere lower thermosphere (MLT) up to the ionospheric E and F regions in the western South American sector. The disturbances were observed during a time interval between 8 and 19 h after the volcano eruption for ionospheric and MLT parameters. The arrival of ground-level atmospheric pressure anomalies was detected 9.4 h after the main explosion for the first wavefront propagating in the west–east direction. In comparison, the second wave from the antipode in the east–west direction arrived 26.6 h after the eruption. The Tonga volcanic eruption injected large amounts of gases, water vapor, and ash into the atmosphere and also produced large pressure perturbations triggering atmospheric waves that propagated from the troposphere to the ionosphere. Powerful volcanic eruptions can trigger severe disturbances that might reach the upper atmosphere and produce periodic waves in both neutral and charged particles. As the waves travel upwards into thinner atmospheric layers, they begin moving at higher velocities (Lognonné et al. 2006). Accordingly, we observe that over the western South American sector, the initial time (~ 12:00–12:30 UT) of most of the ionospheric perturbations in the magnetic field, EEJ, plasma drifts, TEC, attributed to the volcanic eruption occur before the initial perturbation in the atmospheric pressure (~ 13:50 UT), except the Y-forking signature in the ionograms, the MLT neutral wind variation, and a second wave train detected in GNSS dTEC. A representation of the wave propagation and affected parameters is shown in Fig. 13. The approximate initial and end time of detection of these disturbances are shown in Table 3.

Lamb wave propagation

A broad spectrum of waves was produced by the explosive volcanic event, including Lamb waves (Amores et al. 2022). The Hunga Tonga Lamb wave propagated around the globe with a surface phase speed of about 318 m/s and passed through the antipodal point in Algeria 18.1 h after the eruption (Wright et al. 2022). Our measurements showed that the pressure anomaly of the first wavefront, on 15 January 2022, was detected sequentially by the Piura, Jicamarca, and Huancayo stations with an estimated phase velocity of 301.32 ± 1.5 m/s, which is consistent with their distances to the eruption epicenter and it is associated with the Lamb wave propagation.

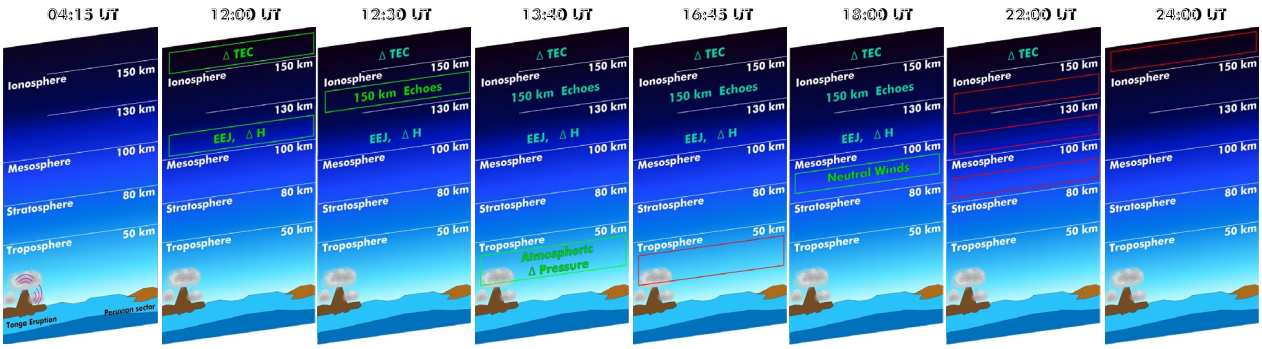

Fig. 13 Wave propagation from the epicenter of the eruption (The Hunga Tonga–Hunga Ha'apai volcano) to the Peruvian sector. The appearance (green) and disappearance (red) times corresponding to perturbations in each measured parameter are shown

Table 3 Approximate initial and end time of perturbations observed in geophysical measurements due to the Tonga volcanic eruption

Measurement	Day—initial time of perturbations UT	Day—end time UT
Atmospheric pressure (Jicamarca 0.5 km altitude)	Jan 15—1340 UT Jan 16—0555 UT	Jan 15—1645 UT Jan 16—0915 UT
H magnetic field component (Jicamarca 0.5 km altitude)	Jan 15—1200 UT	Jan 15—2200 UT
EEJ (100–125 km altitude)	Jan 15—1200 UT	Jan 15—2200 UT
150-km echoes vertical drifts (130–170 km)	Jan 15—1230 UT	Jan 15—2100 UT
Y-forking signature in the ionograms	Jan 15—2013 UT	Jan 15—2200 UT
MLT Neutral winds	Jan 15—1800 UT	Jan 15—2200 UT
TEC variations	Jan 15—1200 UT	Jan 15—2400 UT

This speed estimate is in good agreement with the one calculated by Takahashi et al. (2023) using stations in Chile and Brazil (304 ± 5.6 m/s). However, our estimate is slightly less than the velocity calculated by Wright et al. (2022), 318 m/s. This difference could be produced due to the utilization of worldwide measurements in the investigation by Wright et al. (2022) and the varying local conditions, such as the winds. The next day, the anomaly pressure of the wavefront that was traveling from the antipodal point was detected by the Huancayo and Piura stations first and then by the one at Jicamarca; however, it was expected the pressure fluctuation to be detected at Jicamarca before Piura. This unexpected arrival time sequence was possibly caused by the deformation of the wavefront during the propagation of the waves due to atmospheric and surface processes that involved interaction with the orography (Wright et al. 2022).

Tsunami waves

Carvajal et al. (2022) found that tsunami waves around the Pacific coast differed from those in other parts of the world after the eruption. This tsunami was characterized by small (leading) waves arriving earlier than much larger ones. The leading waves arrived earlier than was theoretically predicted and expected for a tsunami wave freely propagating away from the volcano. They suggested that the leading waves were caused by a fast-moving atmospheric pressure wave with an estimated speed of about 307 m/s, which is the Lamb wave. Kubota et al. (2022) detailed how the Lamb wave contributed to the tsunami waves arriving earlier than expected using simulations. On the other hand, the largest waves possibly originated in the vicinity of the volcano and coincided or occurred systematically after the theoretical travel times of a tsunami freely propagating away from the epicenter. The leading tsunami waves at Matarani and Callao arrived slightly after the atmospheric pressure anomalies, around 14:30–15:30 UT. These times are consistent with measurements from other studies that detected tsunami waves on the South American Pacific coast on the same day (Carvajal et al. 2022; Takahashi et al. 2023; Hu et al. 2023; Ravanelli et al. 2023). Following the leading waves, larger tsunami amplitudes arrived on the Peruvian coast near 19:00 UT. This time is consistent with the theoretical travel time of a free tsunami wave with a mean speed of 198 m/s estimated by Carvajal et al. (2022).

MLT perturbations

The surface Lamb wave propagating at ~ 300–318 m/s was expected to arrive at around 13–14 UT to the west side of the South American continent. In the effort to search for signatures of this wave at the time of arrival in the MLT region using meteor-radar data, we have tried several averaging windows of 5, 15, and 30 min at the expense of losing altitude resolution. We found no indication of such a wave. On the other hand, the clear perturbation at ~ 18 UT on both systems at Jicamarca and Piura can be interpreted as an L1 Lamb-wave mode (Francis 1973). The phase speed of this mode is slower than 300–318 m/s and the perturbation was described in detail by Poblet et al. (2023). They found MLT horizontal wind perturbations with horizontal phase velocity, period and wavelength of about 200 m/s, 2 h, and 1440 km that we confirmed. The L_1 Lamb-wave mode was also found by Liu et al. (2023) in WACCM-X simulations with a phase speed of about 245 m/s. One reason we can see the effects of the second Lamb wave (L_1) in the MLT region and not an effect from the first one might be that it displays its kinetic energy peak in the mesosphere instead of the Earth's surface (Poblet et al. 2023; Francis 1973). An alternative explanation of the MLT wind perturbation near 18 LT could be related to the gravity waves generated by the largest tsunami waves triggered by the eruption that arrived on the Peruvian coast near that LT period. These gravity waves travel faster than the tsunami waves and they might have reached Peru a couple of hours before the arrival of the largest tsunami waves (Poblet et al. 2023) and could have produced TIDs that manifested in TEC perturbations. However, simulations performed by Vadas et al. (2015) showed that tsunami-induced gravity waves are generated in a continuum of frequencies (different propagation speeds) but Poblet et al. (2023) did not find any indication of this polychromatic nature of the disturbances of the neutral winds in the MLT region.

Ionospheric perturbations

Previous studies have detected the occurrence of acoustic-gravity waves after the eruption (Zhang et al. 2022; Wright et al. 2022). Gravity waves produced by the eruption could have perturbed the ionized atmosphere, causing changes in the E- and F-region neutral winds, electron density (Negale et al. 2018), electric fields, and drift velocities. It is known that neutral particles or winds can modify the electric currents in the ionosphere through the ion-neutral coupling and collision effects of neutral and charged particles affecting the E- and F-region dynamos (Heelis 2004). In these regions, the Hall and Pedersen conductivities play important roles. During daytime, the E-region dynamo is dominant and the currents in the direction perpendicular to $\mathbf{B}$ are proportional to $-(\mathbf{U} \times \mathbf{B}) \times \mathbf{B}$ and $(\mathbf{U} \times \mathbf{B})$ at altitudes where the dominant conductivity is the Hall and Pedersen, respectively. The Hall conductivity is greater than the Pedersen conductivity in the E region below about 120 km. In comparison, the Pedersen

conductivity is more significant above 120 km than the Hall conductivity. Wind disturbances due to the eruption then produced perturbations in the electric fields and plasma density that could be reflected in plasma drifts and electron density disturbances or TIDs in the ionosphere. After the eruption, extreme fluctuations in the equatorial electrojet and thermospheric winds were observed by Swarm and ICON, respectively (Harding et al. 2022; Le et al. 2022; Aa et al. 2022). These extreme winds, which reached magnitudes of about 200 m/s, affected the ionospheric electrodynamics in the E and F regions. Effects we observed in the Peruvian ionosphere were detected as perturbations in the EEJ, plasma drifts, and TEC. ICON MIGHTI wind measurements have evidenced that the zonal and meridional winds were not uniform in altitude and time on 15 January 2022 and even reversed direction at certain times and regions. Therefore, the wind disturbances produced by the eruption caused perturbations in the current systems and the generation of polarization charges that affected the ionospheric electric fields.

Plasma drift variations

To our knowledge, this is the first time ground-based radar measurements of ionospheric plasma drifts and EEJ perturbations in the western South American region triggered by the Tonga event are presented. Moreover, this is the first time that the Jicamarca Radio Observatory radar has measured the effects of a volcanic eruption on the equatorial ionospheric electrodynamics over Peru. Using satellite observations, extreme zonal and vertical drifts have also been reported in the Pacific longitude sector, at about 4000 km from Tonga, less than an hour after the eruption and before any atmospheric wave arrived (Gasque et al. 2022). ICON Ion Velocity Meter (IVM) drift measurements for the first orbit following the 15 January 2022 eruption were magnetically connected to the ionospheric E-region at about 400 km from Tonga. This allowed the sampling of the dynamo region close to Tonga within an hour of the main eruption and evidenced a conjugate effect. Previous investigations have studied the conjugacy effect after the eruption and showed the appearance of simultaneous TIDs over Australia (Southern Hemisphere) and the corresponding magnetically conjugate area over Japan (Northern Hemisphere) (Shinbori et al. 2022; Lin et al. 2022). In addition to the TIDs, Shinbori et al. (2022) found plasma flow perturbations of about 100–110 m/s and estimated a zonal electric field of about 2.8–3.1 mV/m. These observations suggest that the expanding wavefront generated strong electric potentials which were transmitted along the magnetic field lines to the northern hemisphere.

Vertical drift variations

Comparing our measurements of the vertical $\mathbf{E} \times \mathbf{B}$ drift and the horizontal magnetic field variation, we found a high Pearson correlation of about 0.94. The variations in the vertical drift follow the changes in the magnetic field proportionally. This feature is consistent with the quantitative linear relationship between the $\mathbf{E} \times \mathbf{B}$ drift and the strength of the EEJ current (Anderson et al. 2002, 2004). We obtained the least-squares, straight line that fits the $\Delta H_{\text{JRO-Piura}}$ vs the vertical $\mathbf{E} \times \mathbf{B}$ drift values to quantify their relationship when both are positive and it is given by $\Delta H_{\text{JRO-Piura}} = 3.194 * \mathbf{E} \times \mathbf{B}$ drift + 12.091. The linear relationship when both are negative is $\Delta H_{\text{JRO-Piura}} = 4.265 * \mathbf{E} \times \mathbf{B}$ drift − 18.236. In addition, the relationship considering all the data sets positive and negative is given by $\Delta H_{\text{JRO-Piura}} = 4.376 * \mathbf{E} \times \mathbf{B}$ drift − 6.978. During daytime, upward vertical drifts (eastward electric field) and westward zonal drifts are expected, as shown by several studies of F-region ion drifts (Fejer et al. 2008, 2013; Pacheco et al. 2010, 2011). However, we observed plasma drift directions that were opposite to the expected ones due to the effects produced by the volcano eruption. The reversal of the zonal electric field locally from eastward to westward generated the unusual daytime downward vertical $\mathbf{E} \times \mathbf{B}$ drift observed from the radar measurements (150-km echoes) between 12:00 and 16:00 UT. Between 16:00 and 18:00 UT, upward vertical drifts indicated the presence of an enhanced eastward electric field that produced larger vertical drifts than the average values for that local time range. Another smaller reversal of the vertical drift (upward to downward) and the zonal electric field (eastward to westward) is observed between 19:00 and 21:00 UT, as shown in Figs. 8 and 9.

In addition to the ICON-MIGHTI wind measurements (Harding et al. 2022; Le et al. 2022; Aa et al. 2022), simulations by Vadas et al. (2023a) showed the occurrence of large-scale wind perturbations in the E and F regions on 15 January 2022. They simulated the primary and secondary atmospheric gravity waves produced by the upward air movement generated by the Tonga volcanic eruption. Furthermore, they obtained large-scale wind changes created by the dissipation of the secondary gravity waves. These satellite measurements, and simulation results, added to our observations and analysis, suggest that large-scale zonal wind perturbations with eastward/outward propagation were the most likely driver for the main observed equatorial vertical and zonal drift variations in the western South American sector. Between 12:00 and 16:00 UT, large eastward enhancements of zonal winds below 120 km (where the Hall conductivity is more dominant than the Pedersen conductivity) could generate a divergence in the zonal current. Subsequently, polarization electric fields may have arisen to

make the current divergence free, creating the reversal of the zonal electric field locally from eastward to westward. This westward electric field at low latitudes away from the equator could then map to the corresponding apex height at the magnetic equator in the Pedersen region, producing a downward $\mathbf{E} \times \mathbf{B}$ drift. The opposite effect could be driven by a westward wind perturbation in the Hall region, between 16:00 and 19:00 UT, generating a strong eastward electric field and an enhanced upward $\mathbf{E} \times \mathbf{B}$ drift, as observed in our ion drift measurements. For our analysis, we assumed that the primary sources of the vertical drift variations were the zonal wind perturbations in the Hall region since the waves produced by the eruption propagated nearly zonally over the western South American sector, and the highest conductivity during the daytime appears in the Hall region. Although the meridional winds could reach significant magnitudes and drive zonal currents in the Pedersen region at latitudes away from the magnetic equator, they are nearly parallel to the magnetic field at the equator. Thus, they would have less influence in generating zonal electric field disturbances at the magnetic equator and low latitudes than the Hall-region zonal winds. Meridional wind disturbances at latitudes away from the equator in the Hall region may have been more relevant in generating perturbations in the vertical electric field that could have a more significant effect on the variations of the zonal drift. In addition, we can notice that the horizontal wind perturbations were much larger than the vertical ones, as shown by the Vadas et al. (2023a) simulation. Therefore, the contribution of the vertical wind perturbations in generating the prominent disturbances of zonal electric fields would not be as significant as that of zonal wind perturbations. Our observations are consistent with the general wind characteristics found in the ICON measurements and simulations that support our interpretation of the ion drift variations.

Zonal drift variations

Some caution should be applied to the results of the zonal drift due to the lower accuracy of the technique used to measure the zonal drift magnitudes compared to the vertical drift. However, they can provide useful information about their direction (Chau and Woodman 2004). Untypical daytime eastward zonal plasma drifts were observed, particularly near 12:00–13:00 UT, 16:00–18:00 UT, and 20:00–21:00 UT, when westward drifts are expected. A possible explanation for the eastward drift during the daytime is the appearance of increased eastward zonal winds ($\mathbf{U}$) in the Pedersen region. In the altitude regions where the Pedersen conductivity is dominant, the zonal winds will produce a vertical current proportional to $\mathbf{U} \times \mathbf{B}$ near the equator. Enhanced eastward winds may increase upward vertical currents, generating polarization charges that can lead to a resultant downward electric field. Therefore, an eastward $\mathbf{E} \times \mathbf{B}$ drift will be produced. This unusual zonal drift behavior is reflected in the eastward zonal drifts we observe during the daytime. Enhanced eastward zonal winds in the Pedersen region that may support our explanation were measured by ICON-MIGHTI over the American longitude sector (Harding et al. 2022; Le et al. 2022; Aa et al. 2022). When the satellite was orbiting near the corresponding longitudes of the western South American sector (90° W to 70° W) and the distance from ICON to Tonga was about the same as the distance from Tonga to Peru, the MIGHTI instrument measured eastward Pedersen winds. Moreover, the simulations by Vadas et al. (2023a) showed large eastward wind perturbations over Peru at 200 km altitude near 12:00 UT and 16:00–18:00 UT that coincide with the time of our observed eastward drifts perturbations during daytime. Meridional wind perturbations at latitudes away from the equator in the Hall region may have contributed to variations in the vertical electric field near the equator, which could have additionally driven zonal drift changes and reversal of direction.

EEJ perturbations

Large electrojet current variations occurred mainly during the unusual vertical $\mathbf{E} \times \mathbf{B}$ drift behavior. Because of the vanishing E-region conductivity at night, the EEJ only responds to wind systems during the day. A combination of migrating tides and conductivity variation causes the mean diurnal variation of the EEJ (Lühr and Manoj 2013). The difference of the magnetic field H-components between Jicamarca and Piura ($\Delta H_{\text{JRO-Piura}}$) and the radar EEJ Doppler shifts detected changes in the EEJ intensity and direction. These measurements showed that the CEEJ (12:00–16:00 UT) and the enhanced EEJ (16:00–19:00 UT) coincided with a westward and an eastward current, respectively. It has been observed that perturbations in the zonal component of the neutral wind can produce variations in the electrojet (Yamazaki et al. 2014, 2021). The reversal of the zonal wind direction in the E-region locally on the Peruvian ionosphere may have changed the direction of the electrojet, producing the counter-electrojet. That also might be associated with the reversal of the zonal electric field locally from eastward to westward. The scale size of the CEEJ disturbance was estimated by Le et al. (2022) to be on the order of $\sim$ 5000 km, considering a CEEJ duration of 3 h. We have estimated that the scale size could be larger ($\sim$ 6400 km) if we consider that the CEEJ lasted $\sim$ 4 h and had a phase speed of $\sim$ 450 m/s. This speed could be estimated from the CEEJ results by Harding et al. (2022) obtained from the Huancayo and Tatuoca (TTB, 1.2° S, 48.5° W)

ground-based magnetometers, knowing the delay of the minimum value of the H component (∼ 2 h) and the distance between the stations (3190 km).

There is evidence that neutral wind perturbations generated by the eruption affected the EEJ. The proposed explanation by Harding et al. (2022) suggests unusual large westward Pedersen winds, measured by ICON-MIGHTI (Englert et al. 2017), as the possible source of the CEEJ. Moreover, Swarm A confirmed the observed perturbations in the EEJ when it crossed the magnetic equator near 15:36 UT (Peruvian sector) on 15 January. An extremely strong westward EEJ (counter-electrojet) was identified during this pass. On the other hand, Le et al. (2022) attributed the presence of the strong eastward turning of zonal wind in the E-region between 100 and 120 km altitude as the possible source of the CEEJ observed in satellite and ground-based magnetometers. We propose that the combined effect of enhanced westward Pedersen-region zonal winds (∼ 140 km altitude) and eastward Hall-region zonal winds (∼ 100–110 km altitude) could produce counter EEJ or westward EEJ after the eruption. During the CEEJ occurrence time (∼ 14 UT), large westward Pedersen and eastward Hall zonal winds were observed in ICON MIGHTI measurements near 140 and 110 km altitude, respectively (Harding et al. 2022; Le et al. 2022; Aa et al. 2022; Aryal et al. 2023). These wind measurements were sampled at about the same distance from the volcano to the Peruvian region. Similar large perturbations were also obtained in simulations of zonal winds near the western South American sector around the time of the CEEJ occurrence (Vadas et al. 2023a; Liu et al. 2023). This evidence supports our proposed mechanism for the CEEJ generation after the eruption. These wind features are consistent with the favorable conditions for westward EEJ observed in previous studies, and the opposite wind directions can enhance the eastward EEJ intensity (Yamazaki et al. 2014, 2021). Although the ICON wind perturbations considered for our analysis were not measured at the low latitudes, we are assuming a similar wind pattern was produced near the Peruvian sector, taking into account that the distances from the satellite (American sector) to Tonga were close to the distance from Peru to the eruption location. Furthermore, simulations of low-latitude winds by Vadas et al. (2023a) showed a wind pattern in very good agreement with the ICON MIGHTI wind measurements at similar distances from the satellite to the epicenter, reinforcing the assumption of the wind pattern for our interpretation.

Geomagnetic storm effect

The Tonga eruption and wave propagation occurred during the recovery phase of a moderate geomagnetic storm that started on 14 January 2022. According to previous studies, the geomagnetic storm of 14 January had minimal impact in the EEJ (Le et al. 2022; Harding et al. 2022). Harding et al. (2022) analyzed the possible effect of penetrating electric fields and stormtime disturbance dynamo on the EEJ variations. They compared the interplanetary electric field (IEF), dawn-to-dusk electric field, with ΔH and found a very low Pearson correlation between 8 and 16 LT. However, 1-h fluctuations in ΔH appear to correlate with the IEF variations and attributed the penetration electric field as a minor source of the perturbations in the EEJ. According to the EEJ and wind signatures they concluded that the effect of the extreme neutral zonal winds is the dominant factor in producing the perturbations on the EEJ. Furthermore, the characteristics of the zonal winds were different from the winds expected as a result of a geomagnetic storm. Thus, the disturbance winds are unlikely the main cause of the extreme winds observed by ICON.

TIDs

The changes in the current systems caused by the wind perturbations due to atmospheric gravity waves produced after the eruption may have induced variations in the distribution of electron densities reflected in TIDs measured by GNSS-TEC and ionograms. TIDs can be induced by atmospheric gravity waves generated by tsunamis (Peltier and Hines 1976; Artru et al. 2005), such as those detected after the Tohoku earthquake on 11 March 2011 (Crowley et al. 2016; Azeem et al. 2017). Ionospheric disturbances triggered by that tsunami were detected in the far-field region several thousand kilometers from the epicenter using GPS-TEC measurements. Crowley et al. (2016) investigated the tsunami-generated TIDs over the United States in a unique scenario where the tsunami was abruptly stopped by the west coast of the U.S. and the source of atmospheric gravity waves was removed. These conditions were similar to those presented on the west coast of South America with the tsunami induced by the Tonga eruption. After the Tohoku earthquake, TIDs were observed at approximately the same time the tsunami reached the U.S. West Coast. The analysis of the TID parameters revealed that the period was 15.1 min, with a horizontal wavelength of 194.8 km and a phase velocity of 233 m/s. Additionally, the measurements demonstrated that the tsunami-generated TIDs persisted for about 4 h over North America and propagated inland about 1500 km from their source on the West Coast. Their analysis suggested that the tsunami was the source of the observed TIDs and atmospheric gravity waves. Azeem et al. (2017) also observed TIDs generated by the same tsunami event on the West Coast of the U.S. with periods, horizontal wavelengths, and horizontal

phase speeds of about 14–30 min, 150–400 km, and 180–260 m/s, respectively. The tsunami wave reached the West Coast of the United States about 10 to 12 h after the earthquake occurred near Japan (05:46 UT). TIDs were first seen at 15:46 UT and the peak activity was observed from 16:30 to 17:30 UT. Signatures of TIDs were mostly absent by 19:15 UT. Our observations of the TIDs duration (~ 4 h) after the tsunami arrival time are consistent with the results of these studies.

Our study identified two groups of TIDs (dTEC amplitude variation). The first dTEC perturbations were detected near 12:00–15:00 UT (~ 8–11 h after the eruption), with the largest amplitude fluctuations near 13:30–14:30 UT, as is more evident at Jicamarca and Huancayo. These disturbances may be related to the Lamb wave L_0, associated with the leading tsunami wave (Carvajal et al. 2022). A second group of dTEC was observed approximately between 18:00 and 22:00 UT, with the largest fluctuations near 19:00–21:00 UT. Phase speeds are estimated by fitting a linear distance equation $d = v * t$, where d is the distance from the eruption center to the GPS receivers, v is the phase speed, and t is the time when the TIDs have been observed since the volcanic eruption (4:15 UT). This second group had an estimated horizontal velocity of ~ 190–220 m/s, periods of ~ 15–40 min, and wavelengths of ~ 170–530 km. A possible explanation for the appearance of TIDs near 18–22 UT (~ 14–18 h after the eruption) could be related to gravity waves generated by the largest tsunami waves triggered by the eruption (Ravanelli et al. 2023;Crowley et al. 2016; Azeem et al. 2017; Inchin et al. 2020). These largest tsunami waves started to reach the Peruvian coast near 19:00 UT. The general characteristics of the periods, horizontal wavelengths, and horizontal phase speeds of our observed TIDs are consistent with those attributed to tsunami sources. More perturbations on GNSS-TEC were identified between 22:00 and 24:00 UT. However, similar disturbances at these hours were observed during more than half of the days of January; hence, we cannot assure that the effects observed on the eruption day from 22:00 UT until midnight are purely due to the volcanic eruption.

Recent studies of TEC variations over South America support the Lamb wave and tsunami-induced gravity waves as possible sources of the perturbations. Ravanelli et al. (2023) analyzed the sea and the so-called co-volcanic ionospheric disturbances (CVIDs) above Chile and Argentina during the first passage of the Lamb wave and the tsunami arrivals between 12:00 and 23:00 UT using GNSS-TEC variations, the Deep-Ocean Assessment and Reporting of Tsunamis (DART), and the UNESCO-IOC sea level measurements. The effects of the Lamb wave and the regular or largest tsunami waves were identified in oceanic and ionospheric data. The passage of the Lamb wave was more visible around 13:40 UT in observations from DART buoys along the coastline of Chile than in the IOC sea level data. Furthermore, the largest tsunami waves arrived near 18:00 UT along the Chilean coast. Clear ionospheric disturbances were observed in TEC variations above Chile and Argentina between 12:30 and 14:30 UT with an apparent horizontal velocity of about 303 m/s. Ravanelli et al. (2023) attributed those ionospheric disturbances to the Lamb wave, considering the TEC disturbance waveforms and phase speed. They showed that the spectral power is consistent with the frequency range of the Lamb waves (Matoza et al. 2022; Nishida et al. 2014). In addition, the authors reported a previous CVID between 11:30 and 12:00 UT with lower TEC variations and a horizontal velocity of about 606 m/s. The origin of this CVID was not clearly identified. One interesting characteristic to notice is that the arrival of this wavefront at distances of 10,400 km was estimated to be around 12:00 UT, which coincides with the onset time of the perturbations in the ion drifts, magnetic field, and EEJ we observe. Therefore, this CVID in TEC could be related to the ionospheric perturbations in our observations. A third CVID between 18:00 and 21:00 UT, detected by Ravanelli et al. (2023), had an estimated horizontal velocity near 200 m/s and a spectral power peak around 0.9 mHz. These disturbances were associated with tsunami gravity waves.

Similar observations using measurements of TEC disturbances (dTEC) in the Chilean and Brazilian sectors, near the south of the Peruvian region (20° S and 70° W), evidenced two wave packets of TIDs in the 11:30–14:00 UT and 16:00–20:00 UT periods (Takahashi et al. 2023). These periods coincide approximately with the occurrence times of our measurements of the two wave packets of dTEC observed at different GNSS stations in the western South American region. Takahashi et al. (2023) found nine TIDS with phase speeds, horizontal wavelengths, and periods of about 275–544 m/s, 330–1174 km, and 20–36 min, respectively. Atmospheric pressure measurements indicated that the Lamb wave arrived in the south of Chile at Futalefu (43.2° S, 71.9° W) at 12:29 UT and had a phase speed of about 304.5 m/s, reaching the Brazilian region at Fortaleza (3.9° S, 38.4° W) at 17:29 UT. The arrival of the largest tsunami waves was detected at Bahia Mansa (40.6° S, 73.7° W) at 17:15 UT, followed by Valparaiso (33.0° S, 71.6° W) and Tocopilla (22.1° S, 70.2° W) at 18:00 UT. According to the evidence, Takahashi et al. (2023) suggested the Lamb wave and the gravity waves induced by the tsunami as possible sources of the ionospheric disturbances.

On the other hand, recent simulation results proposed an alternative interpretation of the generation of

TIDs through the effect of secondary atmospheric gravity waves (Vadas et al. 2023a, b). Vadas et al. (2023a) found that secondary gravity waves were excited by the body forces and heatings created from the dissipation of primary gravity waves triggered by the eruption. The model showed that these secondary waves propagated globally, generating perturbations in the thermospheric wind patterns. Moreover, the simulations showed a good agreement with the ICON-MIGHTI wind measurements. Medium- to large-scale secondary gravity waves had periods of ~ 20 min–7 h, horizontal phase speeds of ~ 100–600 m/s, and horizontal wavelengths of ~ 400–7500 km. In addition, Vadas et al. (2023b) simulated TIDs induced by the secondary gravity waves from the Tonga eruption. They found that the induced medium- and large-scale TIDs had horizontal phase speeds of ~ 100–750 m/s, horizontal wavelengths of ~ 600–6000 km, and ground-based periods of ~ 30 min to 3 h. This proposed explanation for the thermospheric wind pattern perturbations is more consistent with the initial ionospheric large-scale disturbances we observed in the plasma drifts (electric fields) and EEJ that started at about 12:00 UT and lasted about 4 h. Considering that the Lamb wave has a period much shorter than the one observed in these large-scale electric field perturbations, it is less likely that the Lamb wave could have been the main source of these large-scale wind disturbances. Thus, secondary gravity waves may have been one of the most significant sources for generating large-scale electric field perturbations.

Another observed ionospheric perturbation related to the eruption was the so-called Y-forking signature of the ionograms. It was associated with the reflection of the radio waves at different points of the same isoionic surface due to the wide antenna pattern of the ionosonde. This feature and the presence of TIDs propagating through the ionosphere over the ionosonde explain the Y-forking pattern or double reflection at different altitudes for the same frequency. The ionograms could be detecting different phases of the TIDs that are modulating the ionospheric electron density in a relatively close region that is covered by the antenna beam, and the radio waves are reflecting from the ionosphere at different altitudes (Cervera and Harris 2014; Harris et al. 2012; Munro 1953).

A combined effect of volcano-induced Lamb, tsunami, and secondary gravity waves could be a possible explanation for generating the observed TIDs and ionospheric perturbations. However, the complex dynamic processes between the neutral atmosphere (atmospheric waves) and the ionosphere, associated with tsunami events triggered by volcanic eruptions, and the coupling between the Lamb wave and the ionosphere are only partially understood. Further analysis using simulations and physics-based models in the E and F regions of the American sector will be necessary to understand with more detail the complex electrodynamics and the traveling ionospheric disturbances produced by the Tonga volcanic event and quantify the contribution of the Lamb, tsunami, and secondary gravity waves. A theoretical simulation would be necessary to further quantify the neutral wind contribution to the electrodynamics in the Hall and Pedersen regions at different latitudes in the American sector on the eruption day, which is beyond the scope of the current study. Another interesting idea for future work is comparing the results presented with data from additional instruments distributed in South America, such as a continental network of magnetometers, to study the evolution of ionospheric currents during this event. In addition, developing an acoustic wave propagation simulation based on solving the shallow water equations with spectral methods (due to its similarity to Lamb waves) would help estimate the exact arrival time of the perturbations at different stations.

Summary and conclusions

We have studied temporal variations of perturbations associated with the Hunga Tonga–Hunga Ha'apai volcano eruption from the sea surface passing through the mesosphere lower thermosphere (MLT) up to the ionosphere in the western South American sector. Using several types of ground-based instruments, we observed disturbances in the sea level, atmospheric pressure, H magnetic field component, MLT neutral winds, EEJ Doppler shifts, vertical and zonal plasma drifts, TEC, and virtual height of the ionosphere near the Peruvian sector (283° longitude).

The propagation delay of the Lamb wave in the troposphere was 9.4 h approximately from the epicenter of the eruption to the Peruvian sector according to the barometric recordings. The arrival times for the first wavefront near the surface were 13:40 UT (Piura), 13:50 UT (Jicamarca), and 14:00 UT (Huancayo) and are consistent with the distances from the epicenter. The estimated phase velocity of the Lamb wave was 301.32 ± 1.5 m/s. On the other hand, the second wavefront (traveling from the antipode) was expected to be detected first at Huancayo and then at Jicamarca and Piura almost at the same time, but in turn, the Huancayo and Piura stations (06:55 UT) were the first ones to observe the disturbances, followed by the Jicamarca station (07:05 UT). This might be due to the fact that the first wave train was already deformed when it reached its antipodal point (Algeria) due to atmospheric and surface processes (interaction with the orography), as described by Wright et al. (2022).

We observed large electrojet current variations mainly during the unusual vertical $\mathbf{E} \times \mathbf{B}$ drift behavior. CEEJ

occurred over the Peruvian region from 12:00 to 16:00 UT (8 to 12 h after the eruption), as shown in the horizontal magnetic field changes and radar measurements. We attributed the CEEJ to large-scale enhanced eastward zonal winds in the 100–110 km altitude and increased westward winds in the 140–150 km altitude. Opposite wind directions may have provided favorable conditions for eastward EEJ intensity. These wind characteristics are consistent with recent studies of CEEJ (Yamazaki et al. 2021).

The vertical and zonal plasma drifts over Jicamarca on the day of the eruption, obtained from the 150-km radar echoes, significantly deviated from the 5 and 95 percentiles of the four surrounding months. The signatures of the vertical drift are consistent with the variation of the H magnetic component. Downward and upward drifts correspond to the presence of CEEJ and EEJ, respectively. Daytime vertical plasma drifts exhibit unusual downward behavior between 12:00 and 16:00 UT, followed by an upward enhancement between 16:00 and 19:00 UT. Untypical eastward zonal plasma drifts were observed during the day, especially near 12:00–13:00 UT and 16:00–18:00 UT, when typical daytime westward drifts are expected. Our observations and analysis suggest that large-scale zonal wind perturbations with eastward/outward propagation were the most likely driver for the equatorial vertical and zonal drift variations we observed in the western South American sector. The main reason for this drift behavior is that the eruption-related atmospheric disturbance significantly altered the zonal neutral wind temporally and spatially, which in turn altered the dynamo electric field in the Hall and Pedersen regions.

The MLT neutral wind data displayed a change of direction of the zonal wind from eastward to westward above 95 km altitude around 18:00 UT; however, this change is clear between 80 and 100 km altitude in the residual winds for SIMONe Jicamarca. Similar features were observed in MLT wind measurements over Piura, but in this case, the change of the zonal wind from eastward to westward is noticed between 90 and 100 km altitude. This MLT wind perturbation is most likely due to the passage of a second Lamb wave front (L_1), slower than the first one (L_0) (Poblet et al. 2023).

Quasi-periodic oscillations were observed in TEC measurements at different latitudes between 33.4° S and 4.6° N on the Peruvian longitude sector. These TEC variations were detected as TIDs between 12:00 and 22:00 UT with periodicities in the 15–40 min range on 15 January. Two wave trains of TIDs were identified. The first group was observed near 12:00–15:00 UT (~ 8–11 h after the eruption), with the largest amplitude fluctuations near 13:30–14:30 UT. A second wave train was observed between 18:00 and 22:00 UT, with the largest fluctuations near 19:00–21:00 UT. The passage of the Lamb wave near 14:00 UT and the largest tsunami waves near 18:00–22:00 UT coincided with the occurrence of the two main TID wave trains. We suggest that a combined effect of volcano-induced Lamb and tsunami waves may be a possible explanation for generating neutral wind perturbations and the subsequent observed TIDs. However, we cannot rule out the effects of secondary gravity waves propagating over the western South American sector and produced by the volcanic eruption. Additional evidence of TIDs passing over Jicamarca was found in the untypical Y-forking signatures detected in the ionograms from 20:00 UT to 22:00 UT.

Perturbations from the lower atmosphere region produced by the Tonga volcanic eruption could propagate and produce significant disturbances in the upper atmosphere and ionosphere at distances greater than 10,000 km. Different times for the occurrence of disturbances imply the existence of different physical mechanisms of wave propagation and ion–neutral coupling. This event was unique and significant because it was the first time that the Jicamarca Radio Observatory radar observed evidence of volcano-induced ionospheric perturbations over the Peruvian sector, with several ground-based instruments simultaneously measuring the atmosphere at different layers.

The results obtained through this study can be used as a reference for modeling and simulation efforts to try to reproduce the atmospheric response to the Tonga volcanic eruption. Our observations can be compared with physics and numerical-based models that simulate the expected effects in the troposphere, MLT, and ionospheric regions. Atmospheric measurements can help understand the different kinds of waves generated by explosive, impulsive events, such as strong volcanic eruptions, and the propagation mechanisms involved from the sea surface or ground level up to the ionosphere. Another significant contribution of this type of observational study about the temporal evolution of atmospheric perturbations is the detection of ionospheric disturbances prior to tsunami effects. Identifying these disturbances could be helpful in early warning systems to alert the occurrence of hazardous events that may affect maritime and productive activities near the coastal regions.

Supplementary Information

The online version contains supplementary material available at https://doi.org/10.1186/s40623-024-02022-7.

Supplementary Material 1.

Acknowledgements

We would like to thank Percy Cóndor and Edward Arboleda for their help with the ionosonde data scaling, to Dr. Rodolfo Rodriguez from the University of

Piura and to Manuel Piñas and Dr. José Flores from Huancayo Observatory for sharing their barometric data for this study and to Anette De La Cruz for her help with the illustration design.

Author contributions

E.E. Pacheco and J.P. Velasquez participated in the conception and design of the study, as well as in the analysis and interpretation of the measurements used in this scientific research, and in the draft and final manuscript preparation. J.P. Velasquez processed and analyzed the vertical and zonal plasma drift data. R. Flores contributed with the data processing and analysis of the equatorial electrojet data and participated in the draft and final manuscript preparation; the magnetometer data were processed and analyzed by R. Rojas and J.P. Velasquez. J.L. Chau, J.F. Conte, F.L. Poblet and J. Suclupe participated in the MLT winds data processing and analysis, and in the draft and final manuscript preparation, L. Condori was responsible for the barometric data processing and analysis and participated in the draft and final manuscript preparation; G. Fajardo contributed with the GPS TEC data processing and analysis and interpretation of results and participated in the manuscript preparation; K. Kuyeng, D.E. Scipion and M. Milla contributed to the conception, design and critical review of the study and participated in the manuscript preparation. E. Manay participated in the data processing of the 150 km echoes from the radar measurements. All the authors reviewed the results of the manuscript during the draft preparation. All authors have participated in the preparation of the final manuscript.

Funding

The Jicamarca Radio Observatory is a facility of the Instituto Geofísico del Perú operated through an agreement with Cornell University, under Prime Agreement AGS-2213849 from the National Science Foundation.

Availability of data and materials

The data sets corresponding to Jicamarca radar measurements such as the 150-km Echoes data set and the EEJ data set are available at https://www.igp.gob.pe/observatorios/radio-observatorio-jicamarca/madrigal/. The magnetometer and ionogram data sets are available at http://lisn.igp.gob.pe/, the barometer and the SIMONe data sets are available upon request. The ocean sea level data sets are available from the Sea level observing system UNESCO/Intergovernmental Oceanic Commission (IOC) at the site: http://www.ioc-sealevelmonitoring.org/index.php.

Declarations

Competing interests

The authors declare that they have no competing interest.

Author details

[1]Radio Observatorio de Jicamarca, Instituto Geofísico del Perú, Lima, Peru. [2]Present Address: Comisión Nacional de Investigación y Desarrollo Aeroespacial, Lima, Peru. [3]Instituto de Radioastronomía, Pontificia Universidad Católica del Perú, Lima, Peru. [4]Present Address: Leibniz Institute for Atmospheric Physics, Kühlungsborn, Germany.

Received: 31 May 2023 Accepted: 30 April 2024
Published: 28 May 2024

References

Aa E, Zhang S-R, Wang W, Erickson PJ, Qian L, Eastes R et al (2022) Pronounced suppression and X-pattern merging of equatorial ionization anomalies after the 2022 Tonga volcano eruption. J Geophys Res Space Phys 127:e2022JA030527. https://doi.org/10.1029/2022JA030527

Adam D (2022) Tonga volcano created puzzling atmospheric ripples. Nature 602:3. https://doi.org/10.1038/d41586-022-00127-1

Afraimovich EL, Perevalova NP, Plotnikov AV, Uralov AM (2001) The shock-acoustic waves generated by earthquakes. Ann Geophys 19(4):395–409. https://doi.org/10.5194/angeo-19-395-2001

Afraimovich EL, Astafyeva EI, Demyanov VV et al (2013) A review of GPS/GLONASS studies of the ionospheric response to natural and anthropogenic processes and phenomena. J Space Weather Space Clim. https://doi.org/10.1051/swsc/2013049

Amores A, Monserrat S, Marcos M, Argüeso D, Villalonga J, Jordà G, Gomis D (2022) Numerical simulation of atmospheric Lamb waves generated by the 2022 Hunga-Tonga volcanic eruption. Geophys Res Lett 49:e2022GL098240. https://doi.org/10.1029/2022GL098240

Anderson D, Anghel A, Yumoto K, Ishitsuka M, Kudeki E (2002) Estimating daytime vertical ExB drift velocities in the equatorial F-region using ground-based magnetometer observations. Geophys Res Lett 29(12):1596. https://doi.org/10.1029/2001GL014562

Anderson D, Anghel A, Chau J, Veliz O (2004) Daytime vertical E *times* B drift velocities inferred from ground based magnetometer observations at low latitudes. Space Weath 2:S11001. https://doi.org/10.1029/2004SW000095

Artru J, Ducic V, Kanamori H, Lognonné P, Murakami M (2005) Ionospheric detection of gravity waves induced by tsunamis. Geophys J Int 160:840–848. https://doi.org/10.1111/j.1365-246X.2005.02552.x

Aryal S, Gan Q, Evans JS, Laskar FI, Karan DK, Cai X et al (2023) Tongan volcanic eruption induced global-scale thermospheric changes observed by the GOLD mission. Geophys Res Lett 50:e2023GL103158. https://doi.org/10.1029/2023GL103158

Astafyeva E (2019) Ionospheric detection of natural hazards. Rev Geophys 57(4):1265–1288. https://doi.org/10.1029/2019RG000668

Astafyeva E, Maletckii B, Mikesell TD, Munaibari E, Ravanelli M, Coisson P, Manta F, Rolland L (2022) The 15 January 2022 Hunga Tonga eruption history as inferred from ionospheric observations. Geophys Res Lett 49:e2022GL098827. https://doi.org/10.1029/2022GL098827

Azeem I, Vadas SL, Crowley G, Makela JJ (2017) Traveling ionospheric disturbances over the United States induced by gravity waves from the 2011 Tohoku tsunami and comparison with gravity wave dissipative theory. J Geophys Res Space Phys 122:3430–3447. https://doi.org/10.1002/2016JA023659

Calais E, Minster JB (1998) GPS, earthquakes, the ionosphere, and the Space Shuttle. Phys Earth Planet Int 105:167–181. https://doi.org/10.1016/S0031-9201(97)00089-7

Carvajal M, Sepúlveda I, Gubler A, Garreaud R (2022) Worldwide signature of the 2022 Tonga volcanic tsunami. Geophys Res Lett 49(6):e2022GL098153. https://doi.org/10.1029/2022GL098153

Cervera MA, Harris TJ (2014) Modeling ionospheric disturbance features in quasi-vertically incident ionograms using 3-D magnetoionic ray tracing and atmospheric gravity waves. J Geophys Res Space Phys 119:431–440. https://doi.org/10.1002/2013JA019247

Chau JL, Woodman RF (2004) Daytime vertical and zonal velocities from 150-km echoes: their relevance to F region dynamics. Geophys Res Lett 31:17801. https://doi.org/10.1029/2004GL020800

Chau JL, Urco JM, Vierinen J, Harding BJ, Clahsen M, Pfeffer N, Kuyeng KM, Milla MA, Erickson PJ (2021) Multistatic specular meteor radar network in Peru: system description and initial results. Earth Space Sci 8(1):e2020EA001293. https://doi.org/10.1029/2020EA001293

Crowley G, Azeem I, Reynolds A, Duly TM, McBride P, Winkler C, Hunton D (2016) Analysis of traveling ionospheric disturbances (TIDs) in GPS TEC launched by the 2011 Tohoku earthquake. Radio Sci 51:507–514. https://doi.org/10.1002/2015RS005907

Englert CR, Harlander JM, Brown CM et al (2017) Michelson interferometer for global high-resolution thermospheric imaging (MIGHTI): instrument design and calibration. Space Sci Rev 212:553–584. https://doi.org/10.1007/s11214-017-0358-4

Farley DT (1985) Theory of equatorial electrojet plasma waves-new developments and current status. J Atmos Terr Phys 47:729–744. https://doi.org/10.1016/0021-9169(85)90050-9

Fejer BG, Jensen JW, Su S-Y (2008) Quiet time equatorial F region vertical plasma drift model derived from ROCSAT-1 observations. J Geophys Res 113:A05304. https://doi.org/10.1029/2007JA012801

Fejer BG, Tracy B, Pfaff R (2013) Equatorial zonal plasma drifts measured by the C/NOFS satellite during the 2008–2011 solar minimum. J Geophys Res Space Phys 118(6):3891–3897. https://doi.org/10.1002/jgra.50382

Francis SH (1973) Acoustic-gravity modes and large-scale traveling ionospheric disturbances of a realistic, dissipative atmosphere. J Geophys 78(13):2278–2301. https://doi.org/10.1029/JA078i013p02278

Friis-Christensen E, Luehr H, Hulot G (2006) Swarm: a constellation to study the Earth's magnetic field. Earth Planet Space 58:351–358. https://doi.org/10.1186/BF03351933

Gasque LC, Wu YJ, Harding BJ, Immel TJ, Triplett CC (2022) Rapid Volcanic Modification of the E-Region Dynamo: ICON's First Glimpse of the Tonga Eruption. Geophys Res Lett 49(18):e2022GL100825. https://doi.org/10.1029/2022GL100825

Gonzalez W, Joselyn J-A, Kamide Y, Kroehl HW, Rostoker G, Tsurutani B, Vasyliunas V (1994) What is a geomagnetic storm? J Geophys Res Space Phys 99(A4):5771–5792. https://doi.org/10.1029/93JA02867

Harding BJ, Wu Y-JJ, Alken P, Yamazaki Y, Triplett CC, Immel TJ, Gasque CG, Mende SB, Xiong C (2022) Impacts of the January 2022 Tonga volcanic eruption on the ionospheric dynamo: ICON-MIGHTI and Swarm observations of extreme neutral winds and currents. Geophys Res Lett 49:e2022GL098577. https://doi.org/10.1029/2022GL098577

Harris TJ, Cervera MA, Meehan DH (2012) SpICE: a program to study small-scale disturbances in the ionosphere. J Geophys Res 117:A06321. https://doi.org/10.1029/2011JA017438

Heelis RA (2004) Electrodynamics in the low and middle latitude ionosphere: a tutorial. J Atmos Solar Terr Phys 66:825–838. https://doi.org/10.1016/j.jastp.2004.01.034

Heki K (2022) Ionospheric signatures of repeated passages of atmospheric waves by the, (2022) 15 Hunga Tonga-Hunga Ha'apai eruption detected by QZSS-TEC observations in Japan. Earth Planets Space 74:112. https://doi.org/10.1186/s40623-022-01674-7

Hu G, Li L, Ren Z, Zhang K (2023) The characteristics of the 2022 Tonga volcanic tsunami in the Pacific Ocean. Nat Hazards Earth Syst Sci 23:675–691. https://doi.org/10.5194/nhess-23-675-2023

Huang CY, Helmboldt JF, Park J, Pedersen TR, Willemann R (2019) Ionospheric detection of explosive events. Rev Geophys 57(1):78–105. https://doi.org/10.1029/2017RG000594

Immel TJ, England SL, Mende SB, Heelis RA, Englert CR, Edelstein J, Sirk MM (2018) The ionospheric connection explorer mission: mission goals and design. Space Sci Rev 214(1):13. https://doi.org/10.1007/s11214-017-0449-2

Inchin PA, Heale CJ, Snively JB, Zettergren MD (2020) The dynamics of nonlinear atmospheric acoustic-gravity waves generated by tsunamis over realistic bathymetry. J Geophys Res Space Phys 125:e2020JA028309. https://doi.org/10.1029/2020JA028309

Kubota T, Saito T, Nishida K (2022) Global fast-traveling tsunamis driven by atmospheric Lamb waves on the 2022 Tonga eruption. Science 377:91–94. https://doi.org/10.1126/science.abo4364

Kudeki E, Fawcett CD (1993) High resolution observations of 150-km echoes at Jicamarca. Geophys Res Lett 20:1987–1990. https://doi.org/10.1029/93GL01256

Le G, Liu G, Yizengaw E, Englert CR (2022) Intense equatorial electrojet and counter electrojet caused by the 15 January 2022 Tonga Volcanic Eruption: space-and ground-based observations. Geophys Res Lett 49(11):e2022GL099002. https://doi.org/10.1029/2022GL099002

Li W, Zhu H, Feng J, Wu X, Tang J, Zhang Z, Chen J (2023) Asymmetric ionospheric fluctuations over the Circum-Pacific regions following the January 2022 Tonga volcanic eruption. Space Weather 21:e2022SW003213. https://doi.org/10.1029/2022SW003213

Lin J-T, Rajesh PK, Lin CCH, Chou M-Y et al (2022) Rapid conjugate appearance of the giant ionospheric lamb wave signatures in the Northern Hemisphere after Hunga-Tonga volcano eruptions. Geophys Res Lett 49:e2022GL098222. https://doi.org/10.1029/2022GL098222

Liu H-L, Wang W, Huba JD, Lauritzen PH, Vitt F (2023) Atmospheric and ionospheric responses to Hunga-Tonga volcano eruption simulated by WACCM-X. Geophys Res Lett 50:e2023GL103682. https://doi.org/10.1029/2023GL103682

Lognonné P, Garcia R, Crespon F, Occhipinti G, Kherani A, Artru-Lambin J (2006) Seismic waves in the ionosphere. Europhys News 37(4):11–15. https://doi.org/10.1051/epn:2006401

Lühr H, Manoj C (2013) The complete spectrum of the equatorial electrojet related to solar tides: CHAMP observations. Ann Geophys 31:1315–1331. https://doi.org/10.5194/angeo-31-1315-2013

Matoza RS, Fee D, Assink JD et al (2022) Atmospheric waves and global seismoacoustic observations of the January 2022 Hunga eruption. Tonga. Science 377(6601):95–100. https://doi.org/10.1126/science.abo7063

Munro GH (1953) Reflexions from irregularities in the ionosphere. Proc R Soc Lond A 219(1139):447–463. https://doi.org/10.1098/rspa.1953.0159

Negale MR, Taylor MJ, Nicolls MJ, Vadas SL, Nielsen K, Heinselman CJ (2018) Seasonal propagation characteristics of MSTIDs observed at high latitudes over Central Alaska using the Poker Flat Incoherent Scatter Radar. J Geophys Res 123(7):5717–5737. https://doi.org/10.1029/2017JA024876

Nishida K, Kobayashi N, Fukao Y (2014) Background lamb waves in the Earth's atmosphere. Geophys J Int 196(1):312–316. https://doi.org/10.1093/gji/ggt413

Pacheco EE, Heelis RA, Su S-Y (2010) Quiet time meridional (vertical) ion drifts at low and middle latitudes observed by ROCSAT-1. J Geophys Res 115:A09308. https://doi.org/10.1029/2009JA015108

Pacheco EE, Heelis RA, Su S-Y (2011) Super rotation of the ionosphere and quiet time zonal ion drifts at low and middle latitudes observed by Republic of China Satellite-1 (ROCSAT-1). J Geophys Res 116:A11329. https://doi.org/10.1029/2011JA016786

Peltier WR, Hines CO (1976) On the possible detection of tsunamis by a monitoring of the ionosphere. J Geophys Res 81(12):1995–2000. https://doi.org/10.1029/JC081i012p01995

Poblet FL, Chau JL, Conte JF et al (2023) Extreme horizontal wind perturbations in the mesosphere and lower thermosphere over South America associated with the 2022 Hunga eruption. Geophys Res Lett 50(12):e2023GL103809. https://doi.org/10.1029/2023GL103809

Pradipta R, Valladares CE, Doherty PH (2015) Ionosonde observations of ionospheric disturbances due to the 15 February 2013 Chelyabinsk meteor explosion. J Geophys Res 120(11):9988–9997. https://doi.org/10.1002/2015JA021767

Qiu S, Shi M, Wang X, Zhang Z, Soon W, Velasco Herrera VM (2023) An investigation on the ionospheric response to the volcanic explosion of Hunga Ha'apai, 2022, based on the observations from the Meridian Project: the plasma drift variations. Remote Sens 15:4181. https://doi.org/10.3390/rs15174181

Ravanelli M, Astafyeva E, Munaibari E, Rolland L, Mikesell TD (2023) Ocean-ionosphere disturbances due to the 15 January 2022 Hunga-Tonga Hunga-Ha'apai eruption. Geophys Res Lett 50:e2022GL101465. https://doi.org/10.1029/2022GL101465

Savitzky A, Golay JE (1964) Smoothing and differentiation of data by simplified least squares procedures. Anal Chem 36(8):1627–1639. https://doi.org/10.1021/ac60214a047

Schnepf NR, Minami T, Toh H, Nair MC (2022) Magnetic signatures of the 15 January 2022 Hunga Tonga-Hunga Ha'apai volcanic eruption. Geophys Res Lett 49:e2022GL098454. https://doi.org/10.1029/2022GL098454

Shinbori A, Otsuka Y, Sori T et al (2022) Electromagnetic conjugacy of ionospheric disturbances after the 2022 Hunga Tonga-Hunga Ha'apai volcanic eruption as seen in GNSS-TEC and SuperDARN Hokkaido pair of radars observations. Earth Planets Space 74:106. https://doi.org/10.1186/s40623-022-01665-8

Stober G, Kozlovsky LA, Qiao A, Krochin Z, Shi WG, Tsutsumi KJ, Gulbrandsen M, Nozawa N, Lester S, Baumgarten M, Belova KE, Mitchell N (2023) Identifying gravity waves launched by the Hunga Tonga-Hunga Ha'apai volcanic eruption in mesosphere/lower-thermosphere winds derived from CONDOR and the Nordic Meteor Radar Cluster. Ann Geophys 41:197–208. https://doi.org/10.5194/angeo-41-197-2023

Sun YY, Chen CH, Zhang P, Li S et al (2022) Explosive eruption of the Tonga underwater volcano modulates the ionospheric E-region current on 15 January 2022. Geophys Res Lett 49(15):e2022GL099621. https://doi.org/10.1029/2022GL099621

Takahashi H, Figueiredo CAOB, Barros D et al (2023) Ionospheric disturbances over South America related to Tonga volcanic eruption. Earth Planets Space 75:92. https://doi.org/10.1186/s40623-023-01844-1

Themens DR, Watson C, Žagar N, Vasylkevych S, Elvidge S, McCaffrey A et al (2022) Global propagation of ionospheric disturbances associated with the 2022 Tonga volcanic eruption. Geophys Res Lett 49:e2022GL098158. https://doi.org/10.1029/2022GL098158

Vadas SL, Makela JJ, Nicolls MJ, Milliff RF (2015) Excitation of gravity waves by ocean surface wave packets: upward propagation and reconstruction of the thermospheric gravity wave field. J Geophys Res Space Phys 120(11):9748–9780. https://doi.org/10.1002/2015JA021430

Vadas SL, Becker E, Figueiredo C, Bossert K, Harding BJ, Claire Gasque LC (2023a) Primary and secondary gravity waves and large-scale wind changes generated by the Tonga volcanic eruption on 15 January 2022:

modeling and comparison with ICON-MIGHTI winds. J Geophys Res Space Phys 128(2):e2022JA031138. https://doi.org/10.1029/2022JA031138

Vadas SL, Figueiredo C, Becker E, Huba J, Themens DR, Hindley NP et al (2023b) Traveling ionospheric disturbances induced by the secondary gravity waves from the Tonga eruption on 15 January 2022: Modeling with MESORAC-HIAMCM-SAMI3 and comparison with GPS/TEC and ionosonde data. J Geophys Res Space Phys 128(6):e2023JA031408. https://doi.org/10.1029/2023ja031408

Valladares CE, Chau JL (2012) The low-latitude ionosphere sensor network: initial results. Radio Sci 47:RS0L. https://doi.org/10.1029/2011RS004978

Wood AG, Alfonsi L, Clausen LB, Jin Y, Spogli L et al (2022) Variability of ionospheric plasma: results from the ESA swarm mission. Space Sci Rev 218(6):52. https://doi.org/10.1007/s11214-022-00916-0

Wright CJ, Neil Hindley M, Alexander J et al (2022) Surface-to-space atmospheric waves from Hunga Tonga-Hunga Ha'apai eruption. Nature 609:741–746. https://doi.org/10.1038/s41586-022-05012-5

Yamazaki Y, Richmond AD, Maute A, Liu H-L, Pedatella N, Sassi F (2014) On the day-to-day variation of the equatorial electrojet during quiet periods. J Geophys Res Space Phys 119(8):6966–6980. https://doi.org/10.1002/2014JA020243

Yamazaki Y, Harding BJ, Stolle C, Matzka J (2021) Neutral wind profiles during periods of eastward and westward equatorial electrojet. Geophys Res Lett 48(11):e2021GL093567. https://doi.org/10.1029/2021GL093567

Zhang S-R, Vierinen J, Aa E, Goncharenko LP, Erickson PJ, Rideout W, Coster AJ, Spicher A (2022) 2022 Tonga volcanic eruption induced global propagation of ionospheric disturbances via lamb waves. Front Astron Space Sci 9:871275. https://doi.org/10.3389/fspas.2022.871275

Publisher's Note